

Non-thermal Synchrotron Emission and Polarization Signatures during Black Hole Flux Eruptions

FAN ZHOU,¹ JIEWEI HUANG,² YUEHANG LI,¹ ZHENYU ZHANG,³ YEHUI HOU,⁴ MINYONG GUO,^{1,5} AND BIN CHEN^{3,2}

¹*School of physics and astronomy, Beijing Normal University, Beijing 100875, P. R. China*

²*School of Physics, Peking University, No.5 Yiheyuan Rd, Beijing 100871, P.R. China*

³*Institute of Fundamental Physics and Quantum Technology, & School of Physical Science and Technology, Ningbo University, Ningbo, Zhejiang 315211, China*

⁴*Tsung-Dao Lee Institute, Shanghai Jiao-Tong University, Shanghai, 201210, P. R. China*

⁵*Key Laboratory of Multiscale Spin Physics, Ministry of Education, Beijing 100875, P. R. China*

ABSTRACT

In this work, we investigate synchrotron emission and the observational signatures of anisotropic non-thermal electrons during magnetic-flux eruptions in a magnetically arrested disk, using 3D GRMHD simulations. Non-thermal electrons are assumed to be energized from the thermal background through magnetic reconnection, with pitch-angle distributions modeled as beamed or loss-cone types, alongside an isotropic case for comparison. The results show that non-thermal emission can produce pronounced flux outbursts and localized brightening during eruptions, while the associated increase in optical depth can suppress the linear polarization fraction. Introducing pitch-angle anisotropy further reshapes the angular distribution of the intrinsic emissivity and modulates its contribution to various observable signatures. Our results demonstrate that anisotropic non-thermal electrons are essential for a physically complete interpretation of black hole image variability.

Keywords: Supermassive black holes – Black hole physics – Accretion – MHD – Radiative transfer – Radiation mechanisms: non-thermal – Polarimetry

1. INTRODUCTION

The Event Horizon Telescope (EHT) has obtained the highest-resolution images to date of the supermassive black holes M87* and Sgr A* (Akiyama et al. 2019a, 2022a), opening new opportunities to probe fundamental physics and plasma dynamics in the strong-gravity regime (Akiyama et al. 2019b,c, 2022b,c,d; Psaltis et al. 2020; Kocherlakota et al. 2021). Polarization structures of horizon-scale synchrotron emission reveal ordered magnetic fields (Akiyama et al. 2021a, 2024a), whose geometry encodes signatures of the accretion state and even spacetime rotation (Akiyama et al. 2021b, 2024b). Black-hole accretion systems also show variability: multi-wavelength observations of Sgr A* reveal flares

with enhanced emission (Genzel et al. 2003; Ghez et al. 2004; Baganoff et al. 2001; Abuter et al. 2020; Akiyama et al. 2022b) and localized bright spots (Abuter et al. 2018; Bauböck et al. 2020; Wielgus et al. 2022; Abuter et al. 2023); recent time-variable polarized images of M87* implies a non-quiescent flow (Akiyama et al. 2025). These findings necessitate a better understanding of the dynamical behavior of black-hole accretion flows and their millimeter-wavelength emission and imaging properties.

General relativistic magnetohydrodynamic (GRMHD) simulations are now the standard tool for modeling magnetized accretion flows around black holes (Porth et al. 2019). When coupled with general relativistic radiative transfer (GRRT) (Broderick & Blandford 2004; Shcherbakov & Huang 2011; Dexter 2016; Moscibrodzka & Gammie 2018; Pu & Broderick 2018; Younsi et al. 2020; Bronzwaer et al. 2020; Aimar et al. 2024), they successfully reproduce key observational features (Akiyama et al. 2019b,c, 2021b, 2023, 2022b,c,d, 2024b). Various studies suggest that M87* favors a magnetically arrested disk (MAD), in which strong, ordered magnetic flux threads the black hole (Narayan et al. 2003). This configuration naturally accounts for the observed jet

Corresponding author: Yehui Hou
yehuihou@sjtu.edu.cn

Corresponding author: Minyong Guo
minyongguo@bnu.edu.cn

Corresponding author: Bin Chen
chenbin1@nbu.edu.cn

properties (Blandford & Znajek 1977; McKinney & Gammie 2004; Tchekhovskoy et al. 2011; Cruz-Orsio et al. 2022) and spiral polarization patterns (Akiyama et al. 2021a,b, 2024a,b). MADs also exhibit recurrent magnetic-flux eruptions: excess flux accumulated on the horizon is intermittently expelled and later re-accreted (Igumenshchev 2008; Tchekhovskoy et al. 2011; McKinney et al. 2012). These eruptions release magnetic energy, drive turbulence and reconnection, and efficiently heat electrons, boosting the emitted flux, as shown by high-resolution simulations (Porth et al. 2021; Abuter et al. 2021; Ripperda et al. 2022a; Chatterjee & Narayan 2022; Najafi-Ziyazi et al. 2024). MAD flux-eruption events have therefore been proposed as a mechanism for black-hole flares (Dexter et al. 2020; Porth et al. 2021; Ripperda et al. 2022b; Scepi et al. 2022; Jia et al. 2023; Grigorian & Dexter 2024; Antonopoulou et al. 2025; Jiang et al. 2025).

Electrons can be accelerated out of the thermal pool to high energies during flux-eruption events, generating power-law tails (Moscibrodzka & Falcke 2013; Porth et al. 2017; Davelaar et al. 2019). The non-thermal population can substantially alter the synchrotron emissivity, effective optical depth, and both the degree and morphology of polarizations (Yang & Zhang 2018; Fromm et al. 2022; Galishnikova et al. 2023; Tsunetoe et al. 2024). Moreover, the acceleration mechanisms such as magnetic reconnection are intrinsically anisotropic, implying that the accelerated non-thermal electrons should also exhibit anisotropic distributions (Ball et al. 2018; Comisso & Sironi 2019, 2022; Comisso & Jiang 2023; Comisso 2024). Additional processes near the black hole, such as particle escape along open magnetic field lines and the rapid cooling of high-energy synchrotron emitters, can further imprint anisotropic velocity structures (Kunz et al. 2014; Riquelme et al. 2015). Such anisotropies can influence synchrotron emissions and image morphology (Galishnikova et al. 2023; Tsunetoe et al. 2024, 2025; Lai et al. 2025; Yang & Zhang 2018). Taking into account of anisotropic, non-thermal electrons generated from the thermal pool is therefore essential for building physically self-consistent models of MAD flux-eruption events and for interpreting their observational signatures, including polarimetric images and the distinctions between different electron-acceleration mechanisms.

In this work, we perform 3D GRMHD simulations to generate a MAD state around a spinning black hole, and systematically investigate how non-thermal, anisotropic electrons affect the total flux, spatially resolved images, polarization fractions and patterns, during flux-eruption episodes. The electrons are modeled using the $R - \beta$ prescription that relates the electron temperature to the simulated ion temperature and plasma β (Mościbrodzka, Monika et al. 2016). Synchrotron emission profile is produced by a combined population of thermal and non-thermal power-law electrons, with the non-thermal

component assumed to be energized primarily by magnetic reconnections (Ball et al. 2018). For the non-thermal electrons, we further incorporate various beam-like or loss-cone anisotropies that modulate the local emissivity (Lai et al. 2025). We then perform GRRT calculations to generate 230-GHz polarized images for different electron distributions, enabling a detailed assessment of how non-thermal populations and anisotropy influence the resulting observables.

The structure of this paper is as follows. In Sec. 2, we describe the setup and result of GRMHD. In Sec. 3, we construct the electron distributions and the combined emission model. In Sec. 4, we present the GRRT result and analyze the total flux, intensity maps, linear polarization degree and polarization pattern. We summarize the main findings in Sec. 5 and discuss the directions for future work. In the following, lengths and times are expressed in units of $r_g = GM/c^2$ and $t_g = GM/c^3$, where M denotes the central black hole mass; electromagnetic fields are given in Gaussian units.

2. GRMHD SIMULATION

2.1. Basic equations

We model the accreting plasma as a non-self-gravitating magneto-fluid evolving in a fixed black hole spacetime. Its total energy-momentum tensor can be decomposed into matter and electromagnetic parts, $T^{\mu\nu} = T_m^{\mu\nu} + T_{EM}^{\mu\nu}$, with

$$\begin{aligned} T_m^{\mu\nu} &= h u^\mu u^\nu + p g^{\mu\nu}, \\ T_{EM}^{\mu\nu} &= F^{\mu\rho} F_\rho^\nu - \frac{1}{4} g^{\mu\nu} F^{\alpha\beta} F_{\alpha\beta}, \end{aligned} \quad (1)$$

where $h = e + p$ is the comoving-frame ion enthalpy density, with e , p the internal energy density and pressure; u^μ is the bulk four-velocity, and $F^{\mu\nu}$ is the Faraday tensor. In the ideal-MHD limit, the plasma resistivity is set to zero, implying a vanishing comoving electric field: $u_\mu F^{\mu\nu} = 0$.

The dynamical evolution is governed by the GRMHD equations, consisting of (i) local energy-momentum conservation, $\nabla_\mu T^{\mu\nu} = 0$, (ii) particle number conservation, $\nabla_\mu (\rho u^\mu) = 0$ with ρ the rest-mass density, and (iii) the Bianchi identity, $\partial_{[\lambda} F_{\mu\nu]} = 0$. These equations are supplied with an ideal-gas equation of state. Under the adiabatic approximation, the energy density satisfies the polytropic relation $e = \rho + (\hat{\gamma} - 1)^{-1} p$, where $\hat{\gamma}$ is the adiabatic index, taking $\hat{\gamma} = 5/3$ for non-relativistic and $\hat{\gamma} = 4/3$ for relativistic ions.

For convenience, we introduce “pseudo-electromagnetic” fields defined as $E^\mu = F^{t\mu}$, $B^\mu = -(*F)^{t\mu}$. Their relation to the comoving-frame field $b^\mu = -u_\nu (*F)^{\mu\nu}$ is given by $\{E^\mu, B^\mu\} = \{-\epsilon^{t\mu\alpha\beta} b_\alpha u_\beta, b^{[\mu} u^{t]}$, $\{b^t, b^i\} = \{B^\mu u_\mu, (B^i + b^i u^i)/u^t\}$, where i denotes spatial indices. The pseudo-fields differ from the fields measured by space-time normal observers only by a lapse function (Komissarov 2004).

2.2. Numerical setup

We perform three-dimensional GRMHD simulations of Kerr black hole accretion using the code **BHAC** (Porth et al. 2017). The equations are solved in spherical modified Kerr–Schild (MKS) coordinates (McKinney & Gammie 2004), with a spin parameter $a = 0.9375$. The employment of static mesh refinement (SMR) yields an effective resolution of $N_r \times N_\theta \times N_\phi = 384 \times 192 \times 256$. Owing to the scale invariance of the GRMHD equations, the maximum initial mass density is normalized to $\rho_{\max} = 1$ during the simulation. To avoid unphysical vacuum states where the fluid description ceases to apply, numerical floor values are imposed: if $\rho \leq \rho_{\text{fl}} = 10^{-5}r^{-3/2}$ we set $\rho = \rho_{\text{fl}}$, if $p \leq p_{\text{fl}} = 1/3 \times 10^{-7}r^{-5/2}$ we set $p = p_{\text{fl}}$.

The initial equilibrium torus corresponds to the Fishbone–Moncrief solution (Fishbone & Moncrief 1976), with inner radius $r_{\text{in}} = 20$, pressure maximum at $r_{\text{max}} = 40$, and adiabatic index $\hat{\gamma} = 5/3$. A poloidal magnetic field is seeded via the vector potential

$$A_\phi = A_0 \left(\frac{\rho}{\rho_{\max}} - 0.01 \right) \left(\frac{r \sin \theta}{r_{\text{in}}} \right)^3 e^{-r/400r_g}, \quad (2)$$

with all other components vanishing. The normalization constant A_0 is chosen such that the minimum ratio of gas to magnetic pressure satisfies $(p/p_b)_{\min} = 100$, where $p_b = b^2 b_\mu / 2$ is the magnetic pressure. This initialization ensures rapid growth of turbulence and saturation of the magnetorotational instability (MRI). We further introduce the dimensionless magnetization parameter as $\sigma_M = b^2/\rho$. Extremely high values of σ_M can lead to numerical instabilities and unreliable results. To avoid this, we impose a numerical ceiling $\sigma_{M,\text{floor}} = 50$, replenishing plasma in any cells where $\sigma_{M,\text{floor}}$ exceeds this value. For the subsequent analysis, a stricter threshold $\sigma_{M,\text{cut}} = 20$ is adopted, since the MHD approximation itself is expected to break down in strongly magnetized regions (Kulsrud 2005). Zones with $\sigma_M > \sigma_{M,\text{cut}}$ are therefore excluded from the analysis.

2.3. MAD evolution

For clarity of presentation, physical quantities from the simulation are plotted in Cartesian coordinates associated with the spherical Kerr–Schild (KS) system. The $x - z$ plane corresponds to $\phi = 0$ and π , while the $x - y$ plane corresponds to the equatorial plane at $\theta = \pi/2$. The accretion state can be characterized in terms of the mass accretion rate \dot{M} and the horizon-threading magnetic flux Φ_{EH} , defined as (Tchekhovskoy et al. 2011)

$$\begin{aligned} \dot{M} &= \int_{r_h} \rho u^r \sqrt{-g} d\theta d\phi, \\ \Phi_{\text{EH}} &= \frac{1}{2} \int_{r_h} |B^r| \sqrt{\gamma} d\theta d\phi, \end{aligned} \quad (3)$$

where g denotes the determinant of the Kerr metric and γ the determinant of its spatial part; $r_h = M + \sqrt{M^2 - a^2}$ is the horizon radius. We further introduce a dimensionless MAD parameter $\phi_{\text{EH}} = \Phi_{\text{EH}}/\sqrt{\dot{M}}$, which provides a convenient measure of flux accumulation. An accretion flow reaches the MAD state once $\phi_{\text{EH}} \simeq 15$ (Tchekhovskoy et al. 2011).

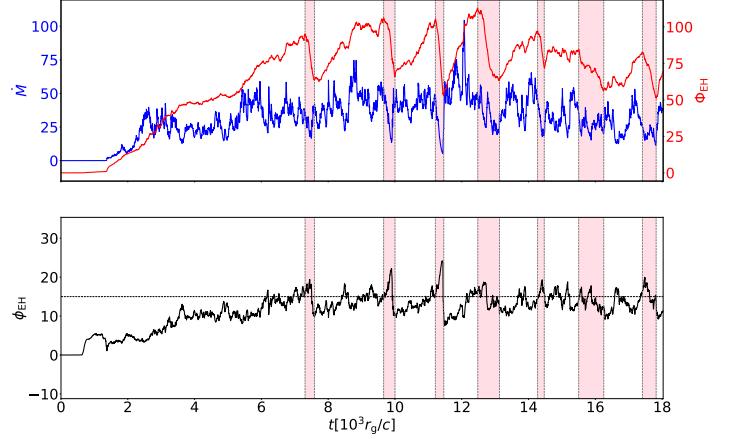


Figure 1. Time evolutions of accretion rate, magnetic flux, and the MAD parameter. The horizontal black line marks $\phi_{\text{EH}} = 15$. We identify flux-eruption events as the pink bands, where Φ_{EH} drops steeply from a local maximum to a subsequent local minimum.

The evolutions of the accretion rate and magnetic flux are shown in Fig. 1. Early on, MRI-driven angular-momentum transport causes the initially equilibrium torus to lose angular momentum and transition into an inflow. Magnetic field lines are advected inward with the plasma and accumulate near the horizon, producing a steady rise in Φ_{EH} . During this phase the flux remains unsaturated, and the system stays in the standard and normal evolution (SANE) state (Akiyama et al. 2019b). Around $t \approx 6000 t_g$, ϕ_{EH} reaches 15, indicating saturation of the poloidal flux near the black hole. The resulting magnetic pressure impedes and partially disrupts the inflow, marking the onset of the MAD state. The flux then undergoes repeated cycles of growth and release. The sharp drops highlighted by the pink bands in Fig. 1 correspond to flux-eruption events (Igumenshchev 2008; Tchekhovskoy et al. 2011; Chatterjee & Narayan 2022), which occur when the horizon-threading flux becomes oversaturated and is rapidly expelled along with matter. After each eruption, the system relaxes to a sub-saturated state, enabling the next cycle of flux buildup and release.

Fig. 2 shows the ion density immediately before, during, and after the third eruption episode ($11210 t_g \sim 11460 t_g$). In the $x - z$ plane, we plot contours of the Bernoulli parameter $-hu_t = 1.05$ (solid curves) and of $\sigma_M = \sigma_{M,\text{cut}}$ (dashed curves), which partition the flow into three zones:

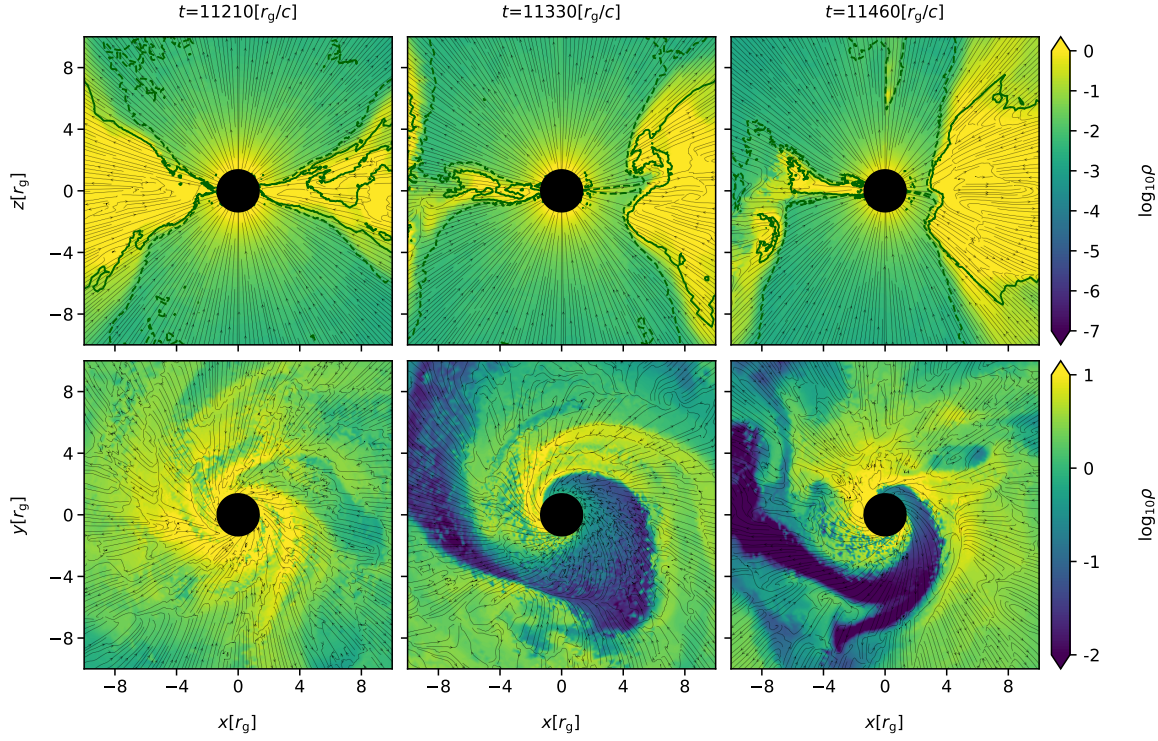


Figure 2. Density profiles in the $x - z$ plane (**top**) and $x - y$ plane (**bottom**) at $t = 11210 t_g$, $t = 11330 t_g$ and $t = 11460 t_g$. The dark green solid contour represents $-hu_t = 1.05$, the dark green dashed contour indicates the magnetization $\sigma_M = 20$, and the black arrows depict the magnetic field lines (the same below).

the disk, with $-hu_t > 1.05$, the jet sheath, with $-hu_t < 1.05$, $\sigma_M < \sigma_{M,\text{cut}}$, and the jet spine, with $\sigma_M > \sigma_{M,\text{cut}}$ (McKinney et al. 2012; Cruz-Orsio et al. 2022), where the plasma becomes sufficiently tenuous to require force-free treatment (Chandra et al. 2015; Chael 2024). Prior to the eruption, the density exhibits a standard, approximately axisymmetric structure. During the eruption, turbulent features develop near the midplane, and the sheath boundaries become strongly distorted. Both the density and magnetic-field morphology indicate that the eruption originates near the equatorial region (Ripperda et al. 2022a; Jia et al. 2023). At peak eruption ($t = 11330 t_g$), a low-density, highly magnetized region with a swirling pattern appears in the $x - y$ plane due to magnetic-pressure release. In the post-eruption stage ($t = 11460 t_g$), the system shows partial recovery, but the outflow retains an asymmetry. The eruption phase is likewise characterized by outward flows, increased magnetization, stronger toroidal magnetic field, and enhanced rotation rate, as illustrated in A.

3. MODELING THE ELECTRONS

3.1. Basic setup

In radiatively inefficient accretion flows, protons and electrons attain different temperatures because Coulomb coupling is weak in the low-density plasma (Akiyama et al. 2019b,c). The proton temperature relates to the gas pressure via $\rho k_B T_p = m_p p_g$. The electron temperature is estimated

using the empirical $R - \beta$ model,

$$\frac{T_p}{T_e} = R_h \frac{\beta^2}{1 + \beta^2} + R_l \frac{1}{1 + \beta^2}, \quad (4)$$

where $\beta = p_g/p_b$ is the plasma- β parameter, with $p_b = b^\mu b_\mu/2$ the magnetic pressure. The constants R_h and R_l set the characteristic proton-electron temperature ratios in strongly and weakly magnetized regions, respectively, thereby modeling the β -dependent coupling (Mościbrodzka, Monika et al. 2016). Synthetic images produced with this prescription match those obtained from magnetic-reconnection-based electron-heating models (Mizuno et al. 2021).

The electron energy spectrum and radiative properties are set by the phase-space distribution measured in the fluid co-moving frame. For a gyrotropic distribution—i.e., isotropic in the plane perpendicular to the magnetic field—the electron distribution function (eDF) is

$$\frac{dn_e}{d\gamma d\Omega} = n_e F(\gamma) G(\alpha), \quad (5)$$

where n_e is the local number density, γ the Lorentz factor, and α is the pitch angle between the electron momentum and the local magnetic field. The functions $F(\gamma)$, $G(\alpha)$ are normalized such that $\int_1^\infty F(\gamma) d\gamma = 2\pi \int_0^\pi G(\alpha) d\cos\alpha = 1$. Note that Eq. (5) assumes a separable form; in general, γ , α are coupled (Galishnikova et al. 2023). For relativistic elec-

trons, however, an expansion in γ^{-1} always yields a separable leading-order term.

Electrons in quiescent accretion disks are often assumed to thermalize into an isotropic Maxwell-Jüttner (MJ) distribution (Jüttner 1911). The mean energy per particle is $m_e f(\Theta_e) \Theta_e$, where $\Theta_e = k_B T_e / m_e$ is the dimensionless temperature and $f(\Theta_e) = (6 + 15\Theta_e)(4 + 5\Theta_e)^{-1}$ is the relativistic correction factor (Gammie & Popham 1998). When the electron relaxation time is short compared to the dynamical timescale, the MJ form is adequate. In weakly collisional flows, however, processes such as reconnection and shocks can accelerate a fraction of electrons, generating a high-energy tail (Moscibrodzka & Falcke 2013; Davelaar et al. 2019). Over a narrow frequency range, the non-thermal electrons can be adequately represented by a single power-law distribution:

$$F_p(\gamma) = \frac{p-1}{\gamma_{\min}^{1-p} - \gamma_{\max}^{1-p}} \gamma^{-p}, \quad \text{for } \gamma_{\min} \leq \gamma \leq \gamma_{\max}, \quad (6)$$

where p is the spectral index. The low-energy cutoff γ_{\min} is typically set at the peak of the MJ distribution, $\gamma_{\min} = 1 + f(\Theta_e) \Theta_e$, while the high-energy cutoff $\gamma_{\max} \sim 10^5$ is determined by microphysical processes (Melzani, Micaëla et al. 2014). Because the results are insensitive to the precise value of γ_{\max} , it is often taken formally to infinity. The mean electron energy is then $m_e \int_{\gamma_{\min}}^{\gamma_{\max}} (\gamma - 1) F_p(\gamma) d\gamma \approx m_e \left(\frac{p-1}{p-2} \gamma_{\min} - 1 \right)$. For reconnection-driven heating, particle-in-cell (PIC) simulations provide an empirical calibration of p in terms of β and σ_M (Ball et al. 2018):

$$p(\beta, \sigma_M) = 1.8 + 0.7\sigma_M^{-0.5} + 3.7\sigma_M^{-0.19} \tanh(23.4\sigma_M^{0.26}\beta). \quad (7)$$

The index decreases with increasing magnetization; for example, $p \approx 5.54$ at $\sigma_M = 2$, and $p \approx 4.84$ at $\sigma_M = 5$. Its dependence on β is rather weak as long as $\beta \gtrsim 0.1$. Because the non-thermal population considered here is generated primarily in eruptive events, turbulent-reconnection heating dominates, and Eq. (7) provides an appropriate characterization.

3.2. Angular dependence

In dynamically strong magnetic fields, weakly collisional electrons readily develop anisotropies. Although the eDF remains gyrotropic, its parallel and perpendicular components can differ substantially (Kulsrud 1983). Studies have shown that such anisotropy can modify the synchrotron spectrum (Yang & Zhang 2018; Lai et al. 2025). It may also imprint observable signatures in mm-band images. To examine anisotropy in a controlled way, we adopt two Gaussian-type prescriptions (Lai et al. 2025). The first is a beam-like distribution, naturally produced by reconnection in relativistic, magnetically dominated plasmas (Comisso & Sironi 2019,

2022; Comisso & Jiang 2023):

$$G_b(\alpha) = \frac{1}{X} \exp\left(-\frac{(\cos \alpha - \cos \alpha_0)^2}{2\sigma^2}\right), \quad (8)$$

$$X = \sqrt{2\pi^3\sigma^2} [\text{erf}(t_2) - \text{erf}(t_1)],$$

$$t_2 = \frac{1}{\sqrt{2\sigma^2}}(1 - \cos \alpha_0), \quad t_1 = -\frac{1}{\sqrt{2\sigma^2}}(1 + \cos \alpha_0),$$

where α_0, σ set the beam center and width, respectively. The values $\alpha_0 = 0$ and π correspond to beams aligned parallel or antiparallel to the magnetic field, respectively. The second distribution is a loss-cone form, representing depleted electron populations along a given direction. Small-pitch-angle electrons on open magnetic field lines could be captured by the horizon, leading to their depletion, while magnetic mirroring suppresses particles moving nearly parallel to the field (Kunz et al. 2014; Riquelme et al. 2015). These effects generate a loss-cone-like eDF, modeled as

$$G_l(\alpha) = \frac{1}{4\pi - X} \left[1 - \exp\left(-\frac{(\cos \alpha - \cos \alpha_0)^2}{2\sigma^2}\right) \right], \quad (9)$$

where $\alpha_0 = 0$ and π yields loss cones oriented parallel or antiparallel to the magnetic field. Radiative cooling can also preferentially deplete large-pitch-angle, high-energy electrons, effectively producing a loss cone centered at $\alpha_0 = \pi/2$, captured by the same functional form in Eq. (9).

Note that the electron distributions in Eq. (8) and Eq. (9) do not possess Z_2 symmetry with respect to the plane normal to the magnetic field (except when $\alpha_0 = \pi/2$), implying direction-dependent acceleration. The specific preferred direction, however, is not known. In the following, we also consider a more conservative Z_2 -symmetrized construction in which the eDF is defined as $\tilde{G}(\alpha) = [G(\alpha) + G(\pi - \alpha)]/2$. We refer to these symmetrized cases as the bi-beam and bi-loss-cone eDFs.

Because the acceleration mechanisms are not precisely known, the fractional contribution of each anisotropic component to the total electron population is uncertain. We therefore treat α_0, σ as free parameters and analyze the synchrotron emission from each eDF in Eq. (8), Eq. (9) and their symmetrized forms separately, without attempting to model any kinetically determined mixtures. A more rigorous treatment is left for future work.

3.3. Anisotropic emissivity

Prior to the imaging analysis, it is useful to examine how the local emissivities behave for different eDFs. Fig. 3 shows the synchrotron emissivities for several fiducial models as functions of the pitch angle α_k . In our notation, \mathcal{B} and \mathcal{L} denote the beam and loss-cone eDFs, respectively; the subscripts \uparrow , \downarrow and \parallel indicate the cases $\alpha_0 = 0, \pi$ and the Z_2 symmetrized configuration, while the subscript \perp indicates $\alpha_0 = \pi/2$; the

labels “1”, “2” refer to $\sigma = 10^{-1}$ and 1, respectively. The parameter choices are summarized in Table. 1.

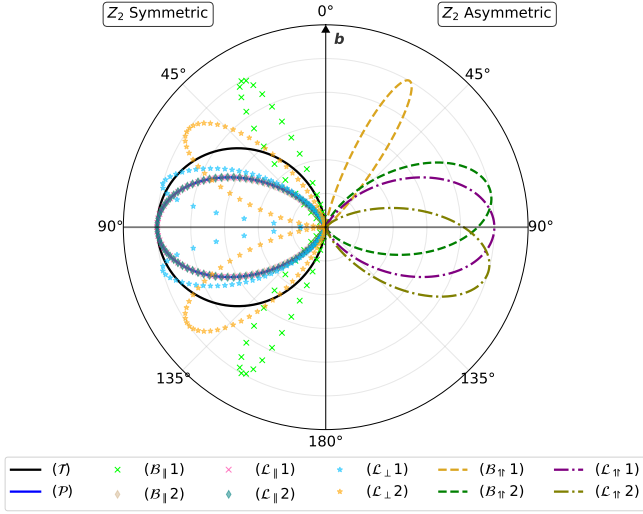


Figure 3. Angular dependence of synchrotron emissivities for eDFs with with (left) and without (right) the Z_2 symmetry, shown as functions of α within the fluid comoving frame. The axis $\alpha = 0^\circ$ denotes the direction of the local magnetic field b .

The angular dependence of the emissivity reflects the combined effects of the single-electron synchrotron pattern and the eDF. A relativistic electron emits strongly along its direction of motion (the headlight effect), and its emissivity is written as $J_\nu^e \approx P_\nu^e(\gamma, \alpha) \delta(\Omega - \Omega_k)$, where P_ν^e is the total radiated power. Integrating J_ν^e over the distribution function Eq. (5) yields the synchrotron emissivity

$$j_\nu(\alpha_k) = n_e G(\alpha_k) \int_1^\infty d\gamma F(\gamma) P_\nu^e(\gamma, \alpha_k). \quad (10)$$

As $\alpha_k \rightarrow 0$ or π , P_ν^e decreases sharply, producing the intrinsic synchrotron anisotropy already visible in the isotropic-eDF results in Fig. 3. Anisotropy in the eDF further modulates the structure of j_ν . For the bi-beam model $\mathcal{B}_{\parallel 1}$, the electrons aligned with the magnetic field suppress emission near the normal plane and generate a double-cone enhancement around $\alpha_k \approx 30^\circ$. For $\mathcal{B}_{\parallel 2}$, the weaker anisotropy is largely overwhelmed by the intrinsic synchrotron pattern, resulting in an emissivity similar to that of \mathcal{P} .

For Z_2 -asymmetric cases, j_ν for $\mathcal{B}_{\parallel 1}$ resembles the one for $\mathcal{B}_{\parallel 1}$ in the northern hemisphere but vanishes in the southern one. The emission from $\mathcal{B}_{\parallel 2}$ is more moderate, with its maximum shifted toward the normal plane. For the loss-cone models, the distribution for $\mathcal{L}_{\parallel 1}$ (and its symmetrized case $\mathcal{L}_{\parallel 1}$) are nearly isotropic, as implied by Eq. (9), yielding emissivities close to \mathcal{P} ; for $\mathcal{L}_{\parallel 2}$, the emissivity peak shifts slightly toward the southern hemisphere. In the bi-loss-cone case $\mathcal{L}_{\perp 2}$, symmetrization smooths both polar cones, again

producing a pattern similar to \mathcal{P} . For $\mathcal{L}_{\perp 1}$ and $\mathcal{L}_{\perp 2}$, the loss cone suppresses emission near the normal plane and generates a weaker double-cone structure reminiscent of $\mathcal{B}_{\parallel 1}$ and $\mathcal{B}_{\parallel 1}$. In what follows, we omit eDFs whose emissivities are degenerate with other cases. We therefore focus on \mathcal{T} , \mathcal{P} , $\mathcal{B}_{\parallel 1}$, $\mathcal{B}_{\parallel 1}$, $\mathcal{B}_{\parallel 2}$, $\mathcal{B}_{\parallel 1}$, $\mathcal{B}_{\parallel 2}$, $\mathcal{L}_{\parallel 1}$, $\mathcal{L}_{\parallel 1}$, and $\mathcal{L}_{\perp 1}$, $\mathcal{L}_{\perp 2}$.

3.4. Combined emission model

Since non-thermal electrons are excited from the thermal background, both thermal and non-thermal synchrotron emission must be included when constructing the emissivity of the accretion flow (Fromm et al. 2022; Akiyama et al. 2022c). The resulting eDF consists of an isotropic thermal component together with a possibly anisotropic non-thermal component, taking the form

$$\frac{dn_e}{d\gamma d\Omega} = n_{\text{th}} \frac{F_{\text{MJ}}(\gamma)}{4\pi} + n_{\text{nth}} F_p(\gamma) G(\alpha), \quad (11)$$

where the subscripts “th” and “nth” denote thermal and non-thermal contributions; $F_{\text{MJ}}(\gamma)$ denotes the Maxwell–Jüttner distribution. The ratio of non-thermal electron energies to the total energies can be read from the PIC simulation (Ball et al. 2018), $\epsilon(\beta, \sigma_M) = A_\epsilon + B_\epsilon \tanh(C_\epsilon \beta)$, where $A_\epsilon = 1 - (4.2\sigma_M^{0.55} + 1)^{-1}$, $B_\epsilon = 0.64\sigma_M^{0.07}$, and $C_\epsilon = -68\sigma_M^{0.13}$. Thus, the number-density ratio can be derived as

$$R = \frac{n_{\text{nth}}}{n_{\text{th}}} = \frac{f(\Theta_e) \Theta_e}{\left[\left(\frac{p-1}{p-2}\right) \gamma_{\min} - 1\right]} \frac{\epsilon}{1 - \epsilon}, \quad (12)$$

where we have sent the upper bound γ_{\max} to infinity. Combining Eq. (12) with the neutrality condition $n_e = n_p = \rho/m_p$, the eDF is fully determined. Thus, the synchrotron emissivity (j_ν), absorptivity (α_ν), and Faraday rotation coefficients (ρ_ν) from thermal and non-thermal electrons are computed as the weighted sums:

$$c_\nu = \frac{1}{1 + R} c_{\text{th}, \nu} + \frac{R}{1 + R} c_{\text{nth}, \nu}, \quad (13)$$

where $c_\nu = \{j_\nu, \alpha_\nu, \rho_\nu\}$. Eq. (13) enhances the contribution of non-thermal particles in regions of high magnetization, consistent with simulated results. For calculating the synthetic images, we use analytical fits for $\{j_\nu, \alpha_\nu, \rho_\nu\}$ corresponding to thermal and power-law eDFs (Dexter 2016; Marszewski et al. 2021). With anisotropy Eqs. (8)–(9), j_ν, α_ν retain closed forms in the ultra-relativistic limit (Leung et al. 2011; Pandya et al. 2016; Galishnikova et al. 2023), as in Eq. (10), so the anisotropic factor enters simply into $G(\alpha_k)$. Faraday rotation coefficients, however, are not analytically tractable for anisotropic eDFs, and we therefore resort to the isotropic-eDF expressions for ρ_ν .

Table 1. Accretion rates for the fiducial eDF models, represented by calligraphic symbols for convenience.

Model	\mathcal{T}	\mathcal{P}	$\mathcal{B}_{\uparrow 1}$	$\mathcal{B}_{\uparrow 2}$	$\mathcal{B}_{\parallel 1}$	$\mathcal{B}_{\parallel 2}$	$\mathcal{B}_{\parallel 1}$
eDF	thermal	thermal + power-law	thermal + beam		thermal + bi-beam		
α_0 (rad)	/	/	0	0	π	π	0 or π
σ	/	/	10^{-1}	1	10^{-1}	1	10^{-1}
\dot{M} ($10^{-4} M_{\odot} \text{ yr}^{-1}$)	5.5	4.5	5.0	4.4	5.6	4.6	5.2

Model	$\mathcal{L}_{\perp 1}$	$\mathcal{L}_{\perp 2}$	$\mathcal{L}_{\uparrow 1}$	$\mathcal{L}_{\uparrow 2}$	$\mathcal{L}_{\parallel 1}$	$\mathcal{L}_{\parallel 2}$	$\mathcal{L}_{\parallel 1}$
eDF	thermal + loss-cone				thermal + bi-loss-cone		
α_0 (rad)	$\pi/2$	$\pi/2$	0	0	π	π	0 or π
σ	10^{-1}	1	10^{-1}	1	10^{-1}	1	10^{-1}
\dot{M} ($10^{-4} M_{\odot} \text{ yr}^{-1}$)	4.6	4.8	4.5	4.8	4.4	4.3	4.5

4. IMAGING RESULTS

The emission profile of the accretion flow is specified by combining the GRMHD output in Sec. 2 with the eDFs introduced in Sec. 3, where we fix $R_1 = 10$ and $R_h = 100$, which falls within the parameter space allowed by the EHT polarimetric constraints (Akiyama et al. 2021b). To generate synthetic images, we perform GRRT calculations using **Coport**, a public code that solves polarized transfer in a covariant framework and incorporates both gravitational and plasma effects (Huang et al. 2024). This code reads the AMR/SMR grids from **BHAC** and interpolates the simulation data along geodesics to compute the Stokes intensities (see Appendix. B for details). The images are ray-traced at 230 GHz with a resolution of 512×512 pixels on an observer's image plane, located at $\theta_o = 17^\circ$ and $\phi_o = 180^\circ$.¹ We adopt the fast-light approximation (Mościbrodzka et al. 2009; Gold et al. 2017), treating each GRMHD snapshot as an instantaneous emissivity field.

4.1. Total flux

The dimensionless GRMHD result should be rescaled to match the case of M87* (Akiyama et al. 2019d), with the scaling determined by requiring the averaged total flux within a quiescent period $t \in [10800 t_g, 11000 t_g]$ to be ≈ 0.66 Jy at 230 GHz. Based on this procedure, we obtain accretion rates for different eDF models, which are summarized in Table 1. Note that we only focus on the third eruption event, as the imaging signatures from different events are qualitatively similar (see Fig. 14).

4.1.1. Effect of emission anisotropy

¹ For an axisymmetric emission profile, the results at 17° and 163° differ only by a reflection symmetry: the intensity and polarization are mirrored across the horizontal axis. In a time-variable flow, minor differences between northern and southern views may appear, but they merely reflect asymmetries about the equatorial plane.

In the purely thermal case \mathcal{T} , the required accretion rate is relativistically higher, whereas for \mathcal{P} it is lower. This difference arises because the observing frequency lies above the thermal synchrotron peak ($\nu_{\text{peak}} \sim 5\Theta_e^2 \nu_B$, where $\nu_B = eB/m_e$ is the cyclotron frequency) leading to suppressed thermal emission. In contrast, the non-thermal high-energy tail radiates efficiently near 230 GHz and remains bright, consistent with previous studies. Consequently, when non-thermal electrons are included, a lower accretion rate and density are sufficient to reproduce the fixed observed flux.

For the anisotropic models, $\mathcal{B}_{\uparrow 2}$, $\mathcal{B}_{\parallel 2}$, $\mathcal{L}_{\perp 1}$, $\mathcal{L}_{\uparrow 1}$, $\mathcal{L}_{\parallel 1}$, and $\mathcal{L}_{\parallel 1}$ have accretion rates similar to \mathcal{P} , owing to their weak anisotropy. In contrast, $\mathcal{B}_{\uparrow 1}$, $\mathcal{B}_{\parallel 1}$, $\mathcal{B}_{\parallel 1}$, $\mathcal{L}_{\uparrow 2}$, and $\mathcal{L}_{\perp 2}$ show higher accretion rates and thus weaker intrinsic emission. This arises largely due to a mismatch between the preferred electron beaming directions (the peak of $G(\alpha)$) and the dominant synchrotron emission directions (the peak of $P_v^e(\alpha)$), which significantly suppresses the intrinsic emissivity.

Moreover, the flux of $\mathcal{B}_{\uparrow 1}$ is clearly higher than that of $\mathcal{B}_{\parallel 1}$, whereas $\mathcal{L}_{\uparrow 2}$ is fainter than $\mathcal{L}_{\parallel 2}$. In the comoving frame, the peak emission of $\mathcal{B}_{\uparrow 1}$ and $\mathcal{L}_{\uparrow 2}$ is directed toward the northern side of the normal plane, while that of $\mathcal{B}_{\parallel 1}$ and $\mathcal{L}_{\uparrow 2}$ points southward (Fig. 3). For a nearly face-on observer, photons are preferentially emitted toward the northern hemisphere with pitch angles below 90° , owing to the split-monopole-like magnetic field in MAD (Fig. 2). As a result, $\mathcal{B}_{\uparrow 1}$ and $\mathcal{L}_{\uparrow 2}$ gain intrinsic emissivity, whereas part of the emissions from $\mathcal{B}_{\parallel 1}$ and $\mathcal{L}_{\uparrow 2}$ is missed, reducing their observed flux. The situation reverses for an observer located near the south polar axis. For brevity, we refer to this effect as directional modulation of anisotropic electron synchrotron emission (DM-AESE).

The above effect can be estimated geometrically by neglecting lensing and bulk-motion aberration. In Cartesian coordinates with the black hole at the origin, the wave vector toward a face-on observer is $\hat{k} = (0, 0, 1)$. For a split-monopole, the field vector takes $\vec{B} \propto (\delta, \cos \theta, \sin \theta)$, where δ is the

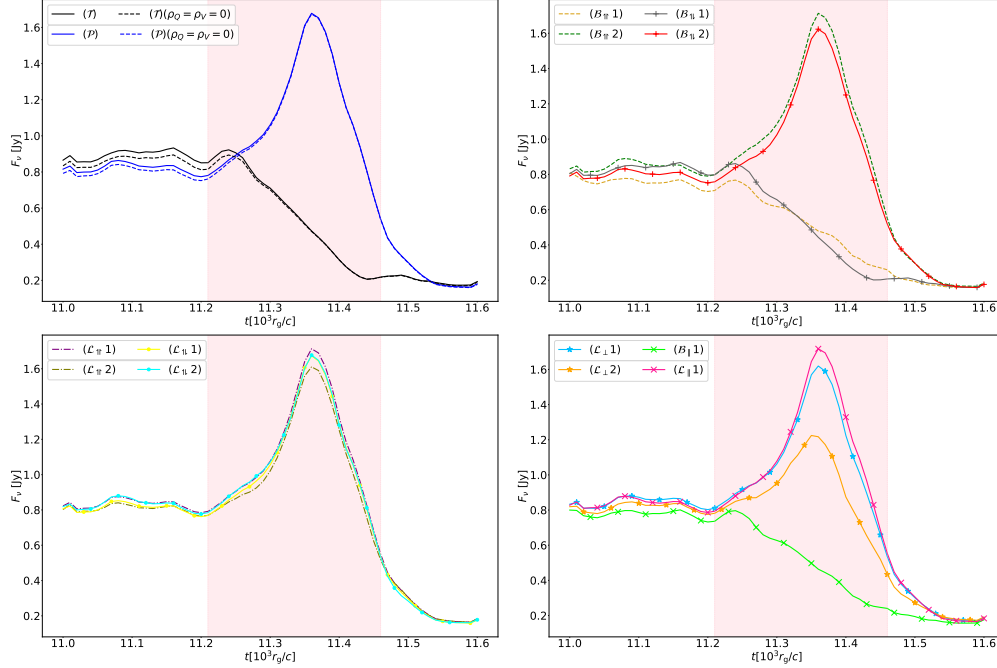


Figure 4. Time evolution of 230 GHz luminous flux for different eDF models. Pink bands indicate the third magnetic flux eruption event.

toroidal-to-poloidal field ratio. For an emission region defined by $(90^\circ - \Delta_e) \leq \theta \leq (90^\circ + \Delta_e)$, the pitch-angle range satisfies

$$\cos^{-1} [\sin \Delta_e (1 + \delta^2)^{-1/2}] \leq \alpha_k \leq 90^\circ. \quad (14)$$

If the emissivity peak falls within this interval, the observed image brightens. In our model, $\Delta_e \lesssim 30^\circ$, and $\delta \sim 0.6 - 1.5$ (inferred from Fig. 13), implying that emissions from $\mathcal{B}_{\parallel} 2$, $\mathcal{L}_{\parallel} 2$ and nearly isotropic eDFs are more easily detected. Although $\mathcal{L}_{\parallel} 2$ and $\mathcal{B}_{\parallel} 2$ have similar angular profiles of j_ν , their absolute amplitudes differ, making $\mathcal{B}_{\parallel} 2$ considerably fainter.

4.1.2. Effect of non-thermal electrons

Fig. 4 shows the time evolution of the 230 GHz total flux. During the eruption, the flux behavior diverges significantly across models. If only thermal electrons are considered (\mathcal{T}), the flux exhibits a pronounced decrease of up to approximately 75%, reflecting the lack of electrons in the low-density region, evacuated by outward magnetic pressure, even though electrons are heated. The fluxes for the strongly beamed cases $\mathcal{B}_{\parallel} 1$, $\mathcal{B}_{\parallel} 1$ and $\mathcal{B}_{\parallel} 1$ exhibit a similar behavior. In these configurations, the non-thermal emission is suppressed not only by the mismatch between the peaks of $G(\alpha)$ and $P_\nu^e(\alpha)$, but also by the misalignment between the dominant emission direction and the photon wave vector, i.e., DM-AESE. Consequently, highly anisotropic non-thermal electrons make only a minor contribution to the total flux.

In contrast, introducing isotropic or moderately anisotropic non-thermal electrons clearly enhances the total flux during

the eruption. As shown in Fig. 4, the models \mathcal{P} (and thus $\mathcal{L}_{\parallel} 1$, $\mathcal{L}_{\parallel} 1$, $\mathcal{L}_{\parallel} 1$), $\mathcal{B}_{\parallel} 2$, $\mathcal{B}_{\parallel} 2$, $\mathcal{L}_{\parallel} 2$, $\mathcal{L}_{\parallel} 2$, and $\mathcal{L}_{\perp} 1$ all exhibit a sharp flux rise followed by a rapid decline, peaking at nearly 1.9 Jy at $t \approx 11360 t_g$, and dropping to about 0.5 Jy by $t \approx 11460 t_g$. Model $\mathcal{L}_{\perp} 2$ also produces a flare, though weaker than \mathcal{P} , due to moderate DM-AESE, as indicated in Fig. 3. These results suggest that during eruptions, the associated population of reconnection-driven, high-energy non-thermal electrons can indeed generate flux enhancements, potentially corresponding to an observed flare state.

In all cases, the post-eruption flux falls below its pre-eruption level. This decline mainly results from reduced magnetization and electron temperature, combined with the disk density not yet recovered, leading to fewer non-thermal electrons, as indicated by Eq. (12). Although the eDF treatment is phenomenological here, it captures the key physics of the decay phase, during which non-thermal electrons cool radiatively and collisionally, gradually returning toward a thermal state.

4.2. Spatially resolved images

Figs. 5, 6 display the total intensity maps (color) and linear polarization pattern (white line segments) for different eDF models during four phases: before eruption, pre-eruption, peak, and post-eruption. In the first two phases, the images are dominated by thermal electrons and exhibit minimal variation across models. During the peak phase, despite a temperature increase as indicated in Fig. 12, the purely thermal model \mathcal{T} produces dimmer images, mainly due to the density decrease.

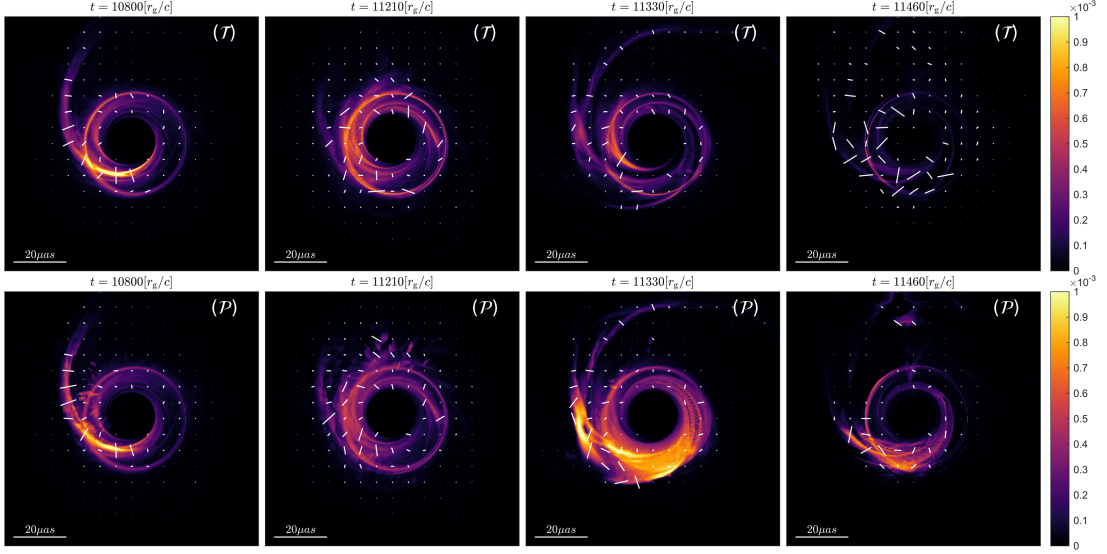


Figure 5. Intensity maps overlaid with linear polarizations at 230 GHz from synchrotron emission of the thermal model \mathcal{T} (**top**) and hybrid model \mathcal{P} (**down**), evaluated at four time instances: $t = 10800 t_g$, $11210 t_g$, $11330 t_g$, and $11460 t_g$ (columns from left to right). The unit of the intensity is $\text{erg s}^{-1} \text{cm}^{-2} \text{sr}^{-1} \text{Hz}^{-1}$.

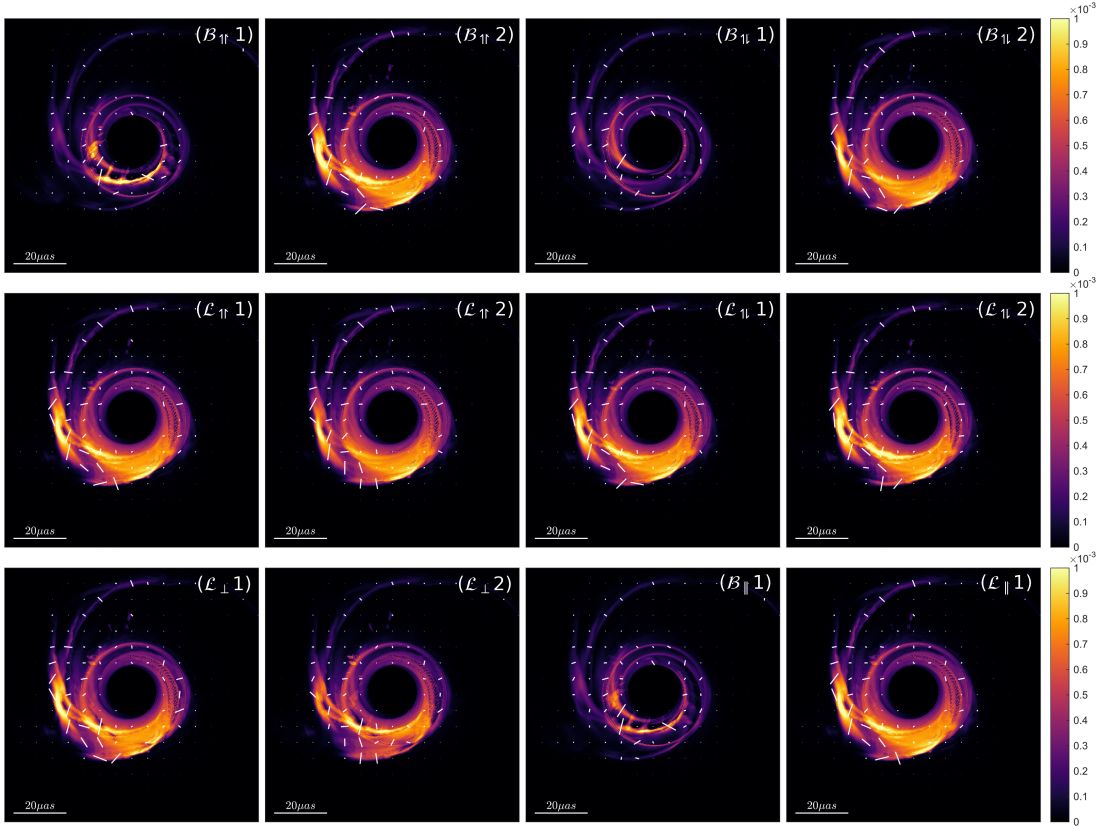


Figure 6. Intensity maps overlaid with linear polarizations at 230 GHz from synchrotron emission of anisotropic eDF models, evaluated at the peak eruption phase $t = 11330 t_g$.

When non-thermal electrons are included, the accretion flow develops a localized brightening in the lower half-plane. This feature arises from the low-density region with enhanced non-thermal emissivity, where the temperature, magnetization, and magnetic field rotation are elevated. In the post-eruption phase, as the temperature and magnetization decrease, both \mathcal{T} and \mathcal{P} models demonstrate reduced brightness, compared to the pre-eruption phase. For anisotropic eDF models, the peak brightness is comparable to isotropic non-thermal electrons, except for $\mathcal{B}_{\parallel 1}$, $\mathcal{B}_{\perp 1}$, and $\mathcal{B}_{\parallel 1}$, which exhibit lower brightness similar to the pure thermal case, consistent with their total flux behavior.

In all plots, the photon ring structure is observed, with a diameter of approximately $40 \mu\text{as}$. This feature is governed by extreme light bending near the photon sphere and has been extensively studied under various gravitational and astrophysical scenarios. The shape and self-similar substructure of sub-rings precisely encode the spacetime information, yet challenging to detect, requiring Earth–Moon–scale baselines (Johnson et al. 2020). In MADs, the plasma self-absorption is non-negligible in the magnetized, high-latitude emission layer (Moscibrodzka & Falcke 2013; Davelaar et al. 2023). After an additional orbital loop, the ray’s intensity is further attenuated. As a result, the observed emission is dominated by a brighter direct image formed during the final passage through the main emitting layer, while higher-order images produced by multiple crossings appear increasingly suppressed.

Close to the horizon, both the streamlines and the magnetic field become strongly twisted due to frame dragging. In particular, the azimuthal angle change diverges as the event horizon is approached (Chen et al. 2025). Following a local brightening triggered during the eruption episode, the brightening is advected inward and forms a luminous, spiraling streamline, as is shown in Fig. 6. Such a spiral morphology can reveal the imprint of spacetime frame dragging and therefore provide a potential test of near-horizon physics (Ricarte et al. 2022; Hou et al. 2025).

4.3. Polarization patterns

In this section, we study the linear polarization (LP) fraction and axisymmetry of the synchrotron emission during the flux eruption, especially their time variabilities.

4.3.1. Optical depths

We first outline how electron emission shapes LP evolution in an accreting plasma. The LP fraction and angle are influenced both by Faraday rotation and plasma’s own emission and absorption. By defining the local LP fraction and angle as $m = I^{-1}\sqrt{Q^2 + U^2}$, $\psi = \arctan(U/Q)$ with I the total intensity, the transfer equation for the linear-part Stokes

parameters $\{Q, U\}$ can be written approximately as

$$\begin{aligned} \frac{dm}{d\lambda} &\approx -\frac{j_I}{I}m + \left[\frac{j_P}{I} - \alpha_P(1 - m^2) \right] \cos(\psi - \psi_P), \\ \frac{d\psi}{d\lambda} &\approx \rho_V - \frac{1}{m} \left(\frac{j_I}{I} - \alpha_P \right) \sin(\psi - \psi_P), \end{aligned} \quad (15)$$

where the LP emissivity and absorptivity are given by $j_P = \sqrt{j_Q^2 + j_U^2}$, $\psi_P = \arctan(j_U/j_Q)$, $\alpha_P = \sqrt{\alpha_Q^2 + \alpha_U^2}$; j_I is the total emissivity, and ρ_V the Faraday rotation coefficient. Circular polarization \mathcal{V} and the Faraday conversion between Q, U and \mathcal{V} are weak (Akiyama et al. 2023), and are neglected here.

For a non-emitting medium, the evolution reduces to the simple relations $dm/d\lambda = 0$, $d\psi/d\lambda = \rho_V$. Once emission and self-absorption are included, ψ acquires an additional rotation, and the mismatch $\psi_P \neq \psi$, together with terms involving j_I, j_P, α_P , generally suppresses m , as indicated by Eq. (15). For instance, even when $\rho_V = 0$ and the solution $\psi = \psi_P$, the LP fraction evolves according to $dm/d\lambda = -(m - j_P/j_I)j_I/I - \alpha_P(1 - m^2)$, where absorption always decreases m , while emission drives it toward j_P/j_I . This emission (absorption)-induced reduction of m provides an important depolarization channel along the ray, which we refer to as dichroic depolarization for short (Rybicki & Lightman 1979).

To assess the optical depths of the rays forming our synthetic images, we plot the image-plane-averaged absorption depth, $\tau_A = \int \alpha_I d\lambda$, and Faraday depth, $\tau_F = \int |\rho_V| d\lambda$ in Fig. 7. The average is weighted by the total intensity at each image-plane pixel. For spatial comparison, we integrate the optical depths separately along segments of each ray that pass through regions with $1 < \sigma_M < 20$ and with $\sigma_M < 1$. The results show that synchrotron emission and absorption arise primarily in magnetized regions with $\sigma_M > 1$, where the Faraday depth is negligible. In contrast, the weakly magnetized, near-equatorial zone ($1 < \sigma_M < 20$) emits little but produces extremely strong Faraday rotation. Together, these features reveal an accretion flow composed of a cold, dense midplane that supplies strong Faraday screening bracketed by hotter, high-latitude emission layers (Moscibrodzka et al. 2017; Ricarte et al. 2020; Davelaar et al. 2023). The emission layers in the thermal model \mathcal{T} remain optically thin throughout the evolution, whereas the hybrid thermal–non-thermal model \mathcal{P} develops higher absorption depth and becomes optically thick during the eruption episode, indicating non-negligible depolarization from dichroic depolarization.

4.3.2. Linear polarization fraction

There are two variables to quantify the averaged LP fraction on the image plane, namely the unresolved, image-integrated LP fractions m_{net} , as well as their resolved, image-averaged

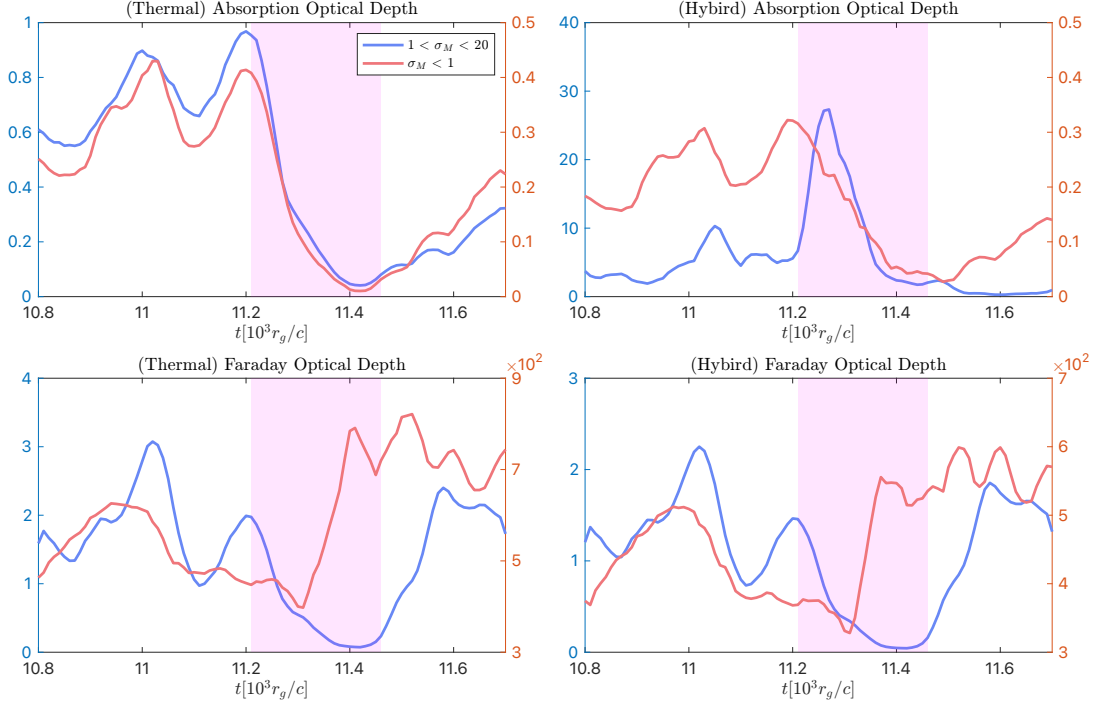


Figure 7. Time evolution of the intensity-weighted, image-plane-averaged absorption optical depth (**top**) and Faraday optical depth (**bottom**) in the thermal (\mathcal{T}) and hybrid (\mathcal{P}) models. For spatial comparison, the optical depths are integrated separately over segments of each ray that traverse regions with $1 < \sigma_M < 20$ and with $\sigma_M < 1$. The purple bands mark the third flux-eruption event.

counterparts $\langle |m| \rangle$:

$$m_{\text{net}} = \frac{\sqrt{(\sum_i Q_i)^2 + (\sum_i \mathcal{U}_i)^2}}{\sum_i I_i}, \quad (16)$$

$$\langle |m| \rangle = \frac{\sum_i \sqrt{Q_i^2 + \mathcal{U}_i^2}}{\sum_i I_i},$$

where i denotes a pixel on the image plane. Note that m_{net} is insensitive to observational resolution, whereas $\langle |m| \rangle$ is not (Akiyama et al. 2021a,b). In synthetic imaging studies, $\langle |m| \rangle$ will converge as the pixel number increases (Pihajoki et al. 2018) and thus can well reflect the resolved LP degree on the observer’s image plane.

We plot $\langle |m| \rangle$ for different eDF models in Fig. 8. Before the eruption, when the fraction of non-thermal electrons is small, the models show minor differences, and $\langle |m| \rangle$ remains at 35% ~ 40%. During the eruption, we observe an enhancement in $\langle |m| \rangle$ for all models. In particular, for the \mathcal{T} , $\mathcal{B}_{\parallel 1}$, $\mathcal{B}_{\perp 1}$ and $\mathcal{B}_{\parallel 1}$ models, $\langle |m| \rangle$ reaches about 60% near $t = 11400 t_g$. The increase can be attributed to the expulsion of matters by the outward magnetic pressure, which reduces emissivity and self absorption (Fig. 7), thus reducing the dichroic depolarization along a light ray.

For the model \mathcal{P} , $\langle |m| \rangle$ exhibits a plateau before a subsequent enhancement, with the transition occurring near $t = 11360 t_g$ —coinciding with the peak of the total flux. It is partially attributed to the transition between optical thin and

thick state (Tsunetoe et al. 2024), as indicated in Fig. 7. During the earlier stage of the eruption, the absorption becomes strong as a result of the enhancement of non-thermal electrons emission. Thus, the plasma becomes optically thick with a typical local LP degree of $\Pi = 3(6p + 13)^{-1}$, which is smaller than that of optically thin case, where $\Pi = (p + 1)(p + 6/3)^{-1}$ (Rybicki & Lightman 1979)². In the later stage of eruption, the plasma return to optically thin and the LP degree increases clearly.

The top-left panel also compares the cases with zero and nonzero Faraday coefficients. We find that the Faraday effect suppresses $\langle |m| \rangle$, particularly prior to the eruption. From Eq. (15), one infers that a larger ρ_V increases the mismatch between ψ and ψ_P , thereby strengthening the dichroic depolarization. Conversely, when ρ_V is very small, ψ and ψ_P remain nearly aligned throughout propagation, which greatly limits depolarization. This behavior is also reflected in the enhanced LP fraction at the end of the eruption, where the Faraday optical depth approaches zero.

For most of anisotropic-electron models, their polarization behavior still tends to resemble that of the \mathcal{T} or \mathcal{P} cases, anal-

² Beside, according to Eq. (7), an increase in magnetization leads to a smaller power-law index, which also results in a decrease/increase in Π for optically thin/thick plasma. For anisotropic eDFs, the intrinsic LP fraction should be modified by the energy dependence of the electron anisotropy (Comisso & Jiang 2023).

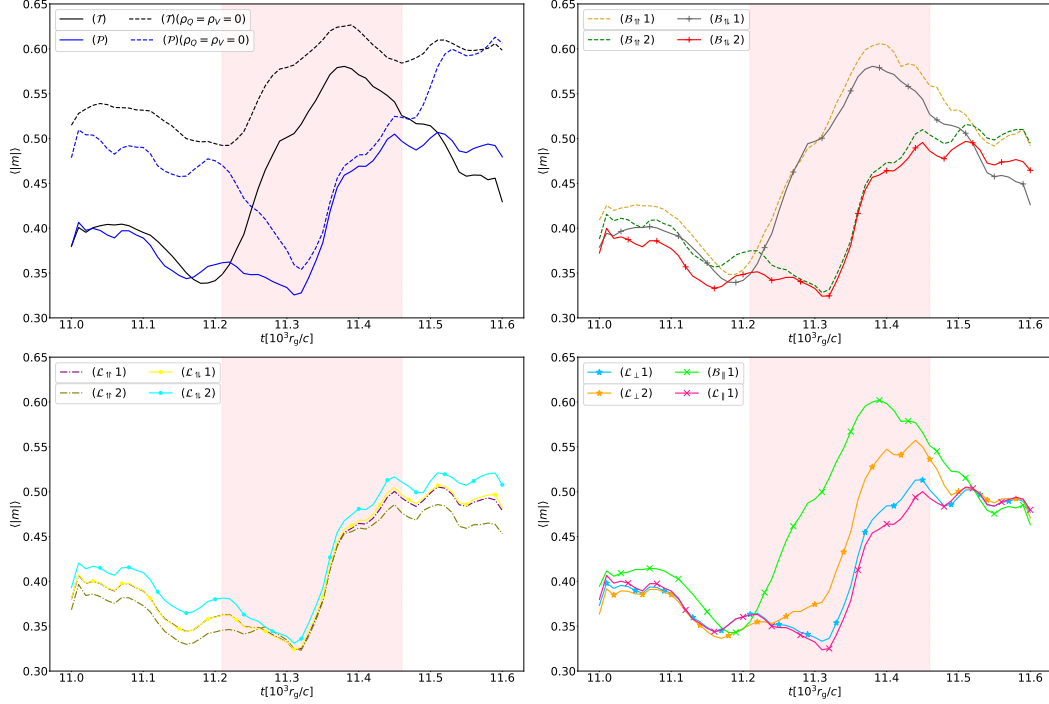


Figure 8. Time evolution of the LP fraction $\langle |m| \rangle$, evaluated for different eDF models. Pink bands indicate the third flux eruption event.

ogous to the situation for the flux. However, both the flux and polarization fraction of $\mathcal{L}_{\perp 2}$ lie between those of \mathcal{T} and \mathcal{P} , further indicating that its corresponding electron anisotropy produces the most prominent observational signatures.

4.4. Second azimuthal Fourier mode

We further characterize the polarization structure using the secondary azimuthal Fourier mode of the linear polarization (Palumbo et al. 2020). It is defined by integrating the complex Stokes parameter $\mathcal{P} = Q + i\mathcal{U}$, weighted by an azimuthal phase factor, over an annulus on the image plane:

$$\beta_2 = \frac{1}{\mathcal{I}_{\text{ann}}} \int_{\rho_{\min}}^{\rho_{\max}} \int_0^{2\pi} \mathcal{P} e^{-2i\phi} \rho d\rho d\phi, \quad (17)$$

where (ρ, ϕ) are polar coordinates, ρ_{\min}, ρ_{\max} define the annulus boundaries, and \mathcal{I}_{ann} is the total intensity within it. The magnitude $0 \leq |\beta_2| \leq 1$ measures the azimuthal order of the polarization field, while the phase $\arg(\beta_2)$ encodes the dominant electric-vector position angle (EVPA) orientation (Palumbo et al. 2020; Akiyama et al. 2021b). For a narrow, axisymmetric ring viewed face-on, one recovers the quadrupolar relation $\arg(\beta_2) = 2 \text{EVPA}|_{\phi=0^\circ}$.

4.4.1. Image-integrated results

In Figs. 9 and 10, we show the temporal evolution of $|\beta_2|$ and $\arg(\beta_2)$, integrated over the full image domain. Several distinct trends emerge. In the thermal model \mathcal{T} , $|\beta_2|$ exhibits a pronounced peak: it rises from 0.2 to 0.4 at $t \approx 11280 t_g$, and then declines to about 0.1 at later times. The case with zero

Faraday rotation also increases during this interval, though more moderately, reflecting reduced dichroic depolarization and thus more intrinsically ordered polarization.

In the \mathcal{P} model, $|\beta_2|$ with and without Faraday effects both show an initial decline followed by a recovery during the eruption. Both minima coincide with the epoch of peak total flux. Because $|\beta_2|$ is weighted by the local intensity, its evolution is dominated by the brightening in the lower half of the image. At the flux maximum, this strongly emitting region—rich in non-thermal electrons and optically thick—produces more disordered polarized emission, leading to the observed minimum in $|\beta_2|$. By the end of the eruption, although the local LP fractions remain high, turbulence and deformation in the re-accreting material increase line-of-sight variations in Faraday rotation, reducing the coherence of the polarization pattern and suppressing $|\beta_2|$ across all eDF models.

The phase $\arg(\beta_2)$ remains positive in all models ($20^\circ \sim 120^\circ$), consistent with previous results for prograde MAD inflows (with sign reversal expected for observers near the southern pole). As shown in Fig. 7, the dominant emission arises from the magnetized layer above the equatorial plane, where the Faraday depth is modest, so $\arg(\beta_2)$ primarily reflects the intrinsic magnetic geometry. The dense equatorial layer, though Faraday-thick, contributes negligible emission and therefore does not influence the integrated phase.

For most of the period following the onset of the eruption, $\arg(\beta_2)$ steadily declines from about 70° to 30° across all models, reflecting the emergence of toroidal magnetic fields in the emission region, as indicated by Fig. 13. This behav-

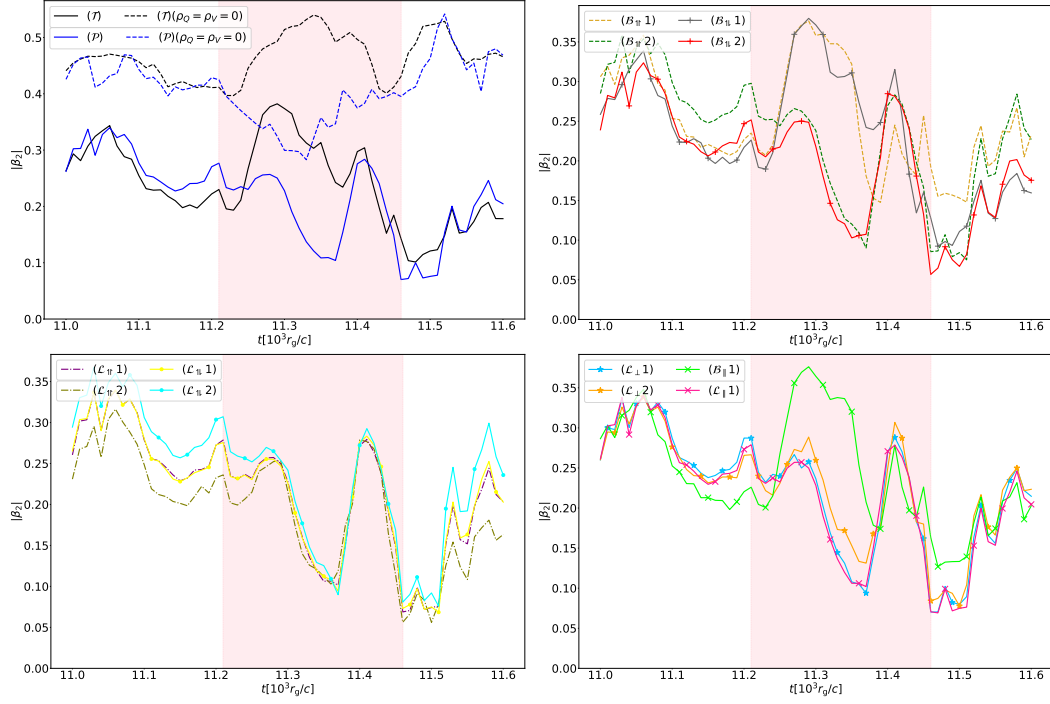


Figure 9. Time evolution of image-integrated $|\beta_2|$, evaluated for different eDF models. Pink bands indicate the third flux eruption event.

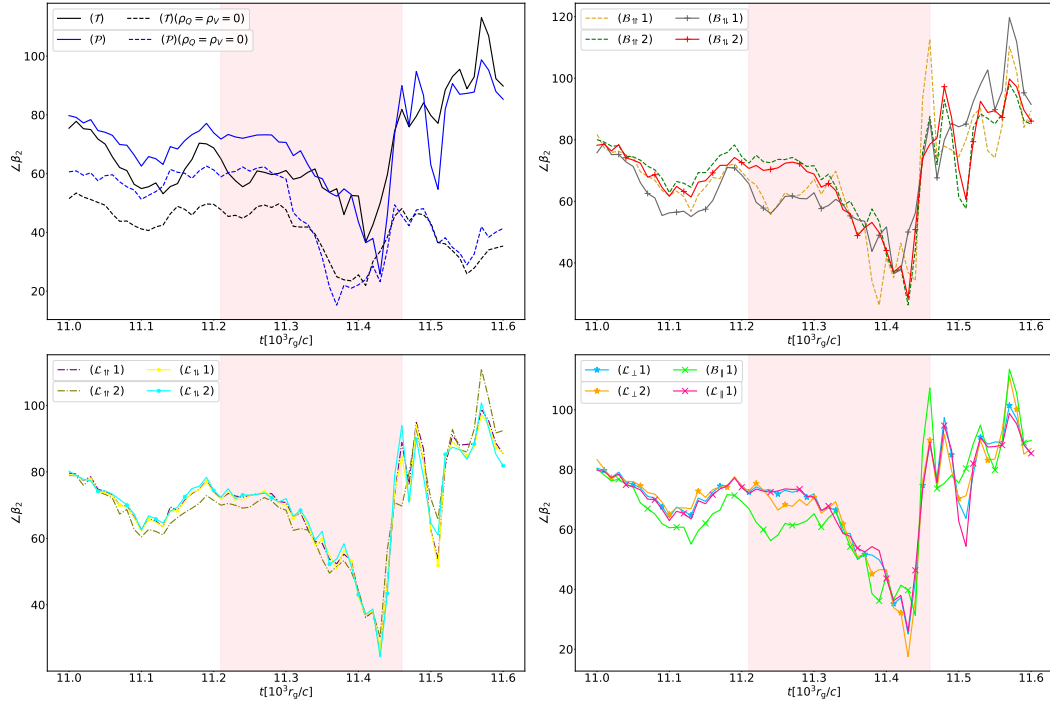


Figure 10. Time evolution of image-integrated $\arg(\beta_2)$, evaluated for different eDF models. Pink bands indicate the third flux eruption event.

ior can be understood as follows: for a near-axis observer, the projected linear polarization vectors are approximately orthogonal to the local magnetic field (neglecting plasma motion and propagation effects). A smaller EVPA therefore corresponds to a more radial polarization pattern, implying a field configuration dominated by toroidal components.

Toward the end of the eruption, $\arg(\beta_2)$ increases markedly, implying a recover of poloidal field as well as the Faraday rotation, as can be inferred from the results of \mathcal{T}, \mathcal{P} with and without ρ_Q, ρ_V . In most eDF models, this enhancement approaches 90° , whereas in models that incorporate a substantial population of beam electrons streaming along field lines ($\mathcal{B}_{\parallel 1}, \mathcal{B}_{\parallel 1}$), $\arg(\beta_2)$ can rise to 110° .

4.4.2. Annular decomposition

Typically, the integration over β_2 is performed across the entire image plane. Here, we relax this constraint and allow ρ_{\min}, ρ_{\max} to be chosen freely, which enables us to examine the detailed polarization patterns influenced by the flux eruption. Fig. 11 presents the temporal evolution of the radial profile of $\arg(\beta_2)$ in the \mathcal{T} and \mathcal{P} models. Results of other eDF models do not exhibit remarkable or enlightening features, and are included in the Appendix. C for completeness. When Faraday coefficients are turned off, the polarization angle exhibits two time-independent regions of steady decline in the \mathcal{T} model: one located at the lensing band ($16 \sim 20 \mu\text{s}$), and the other close to the event horizon ($\lesssim 15 \mu\text{s}$).

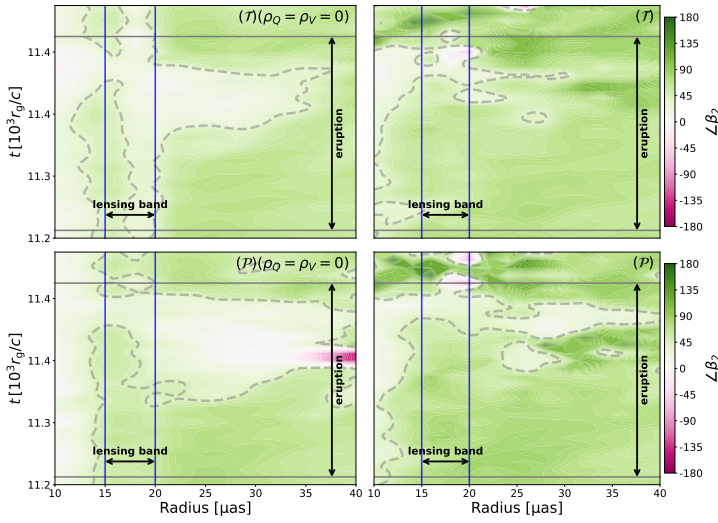


Figure 11. Radial profiles of $\arg(\beta_2)$ for \mathcal{T}, \mathcal{P} models, evaluated as a function of image-plane radius and examined over different evolution times. The left columns present the results with the Faraday coefficients artificially set to zero, while the right columns show the full results including Faraday effects. The blue lines delineate the lensing band, defined by null geodesics that cross the equatorial plane twice before reaching the observer. The dashed contours enclose regions where $\arg(\beta_2) \leq 40^\circ$ in the \mathcal{T} model and $\arg(\beta_2) \leq 45^\circ$ in the \mathcal{P} model.

The lensing-band region corresponds to light rays that cross the equatorial plane twice, so the net polarization reflects the superposed Stokes parameters accumulated over two passages through the emitting region, corresponding to the direct and lensed images (Johnson et al. 2020). In the \mathcal{T} model, where the optical depth is small, both the direct and lensed images contribute appreciably, yielding a clear feature in $\arg(\beta_2)$ across the lensing band. In contrast, the much larger optical depth in the \mathcal{P} model suppresses the lensed-image contribution; the total polarization is dominated by the primary image, and the variation of $\arg(\beta_2)$ across the lensing band is therefore less pronounced.

When the Faraday coefficients are included, the strong equatorial Faraday screen induces substantial polarization-angle rotation along the ray path (Moscibrodzka et al. 2017; Ricarte et al. 2020), and the coefficients further enhance depolarization through Eq. 15 as the ray traverses the entire plasma. As a result, the lensing-band feature in the $\arg(\beta_2)$ profile becomes invisible for all eDF models.

In the region close to the event horizon, frame dragging generates a strong toroidal magnetic field, producing a very small EVPA for near-axis observers—a generic property of magnetized accretion flows. Because this field-dominated polarization signature originates primarily from the main emission layers through the primary image, it is only weakly sensitive to optical-depth effects, yielding similar behavior in both the \mathcal{T} and \mathcal{P} models.

5. SUMMARY AND DISCUSSION

In this work, we have investigated the 230 GHz imaging and polarization signatures produced by synchrotron emission from non-thermal electrons in a MAD during a flux-eruption event. We performed a 3D GRMHD simulation of a MAD around a Kerr black hole, identifying the flux eruption by the rapid drop of the horizon-threading magnetic flux from a local maximum to a subsequent minimum (Sec. 2.3).

To analyze the emission properties, we constructed a phenomenological hybrid thermal–non-thermal eDF model (Sec. 3). Nonthermal electrons were assumed to be energized from the thermal pool via magnetic reconnection, forming a power-law tail whose index and energy fraction followed fitting functions from existing PIC. We have also introduced a Gaussian function with adjustable center and width to model possible pitch-angle anisotropies, allowing for beam like or loss-cone distributions (Sec. 3.2).

We have examined the local emissivity for different eDFs and found that the combination of single-electron emission anisotropy and eDF anisotropy significantly modified the emissivity, even producing a double-cone structure (Sec. 3.3). We then performed GRRT calculations to generate 230 GHz images for several fiducial eDF models, focusing on the evolution of total intensity and polarization throughout the

flux-eruption episode (Sec. 4). The GRMHD outputs were rescaled such that the pre-eruption total flux matched 0.66 Jy for the near-axis observer with $\theta_o = 17^\circ$, consistent with M87* observations. Our main findings are summarized as follows:

- Introducing a non-thermal eDF (\mathcal{P} , $\mathcal{B}_{\parallel 2}$, $\mathcal{B}_{\perp 2}$, $\mathcal{L}_{\parallel 1}$, $\mathcal{L}_{\perp 1}$, $\mathcal{L}_{\parallel 2}$, $\mathcal{L}_{\perp 2}$, $\mathcal{L}_{\perp 1}$, $\mathcal{L}_{\perp 2}$) can indeed enhance the total flux during the eruption, demonstrating that non-thermal electrons play a non-negligible role in black-hole flaring states (Sec. 4.1.2). Even modest changes in the non-thermal fraction efficiently modify the 230 GHz emissivity.

- A localized brightening emerges on the image plane as the flux outburst develops, corresponding to low-density, high-temperature, highly magnetized regions with higher non-thermal electron population (Sec. 4.2). This brightening also leaves imprints on the image-integrated pattern of $|\beta_2|$ (Sec. 4.4.1).

- Moderately anisotropic nonthermal eDF models are indistinguishable from the isotropic nonthermal one \mathcal{P} , whereas strongly anisotropic eDFs (such as $\mathcal{B}_{\parallel 1}$, $\mathcal{B}_{\perp 1}$, $\mathcal{B}_{\parallel 1}$) can suppress the non-thermal emissivity toward the near-axis observer and reshape the 230GHz image morphology in a way that renders them largely degenerate with the thermal model \mathcal{T} (Sec. 4.1.1).

- The linear-polarization fraction in the thermal model (\mathcal{T}) increases during eruption due to reduced density and optical depth, whereas that in the hybrid model (\mathcal{P}) decreases, as enhanced non-thermal emissivity raises the local optical depth, producing strong dichroic depolarization (Sec. 2.3).

- The image-integrated polarization orientation $\arg(\beta_2)$ decreases during eruptions in all models, reflecting the growing dominance of the toroidal field component (Sec. 2.3). In the radial profile of $\arg(\beta_2)$, the strong-lensing signature is blurred by optical depth and by the equatorial Faraday screen, especially in model \mathcal{P} model, where the emission region is nearly optically thick. The frame-dragging-induced near-horizon feature remains potentially observable despite in-medium effects (Sec. 4.4.2).

In conclusion, our results show that both the non-thermal electron population and its anisotropy play distinct roles in

shaping the observed variability during MAD flux-eruption events. Non-thermal electrons can drive flux outbursts and localized brightening on the image plane, while reducing the linear-polarization fraction by increasing the absorptive optical depth along the line of sight. The anisotropy of the eDF reshapes the angular distribution of the intrinsic emissivity and modulates the observability of non-thermal electrons. Together, these effects provide a coherent and physically motivated framework for diagnosing the accretion state and probing the underlying plasma processes through light-curve and polarimetric observations (Algaba et al. 2024).

Several physical processes lie beyond the scope of this study. Under the fast-light approximation, emission is projected instantaneously onto the image plane, neglecting light-travel-time differences. Including these delays in a slow-light treatment introduces a characteristic lag of order $\sim \frac{\pi}{2} (\tilde{r}_0)^2$ between the lensed and direct images, where \tilde{r}_0 is the face-on photon-sphere radius. Rapid fluid variability may also induce radiation perturbations that imprint observable substructure in the direct image.

Although anisotropy plays a minor role in the flux and polarization for near-axis observers such as at $\theta_o = 17^\circ$, this does not imply that its influence remains small at larger viewing angles, where the observer could intercept more directional non-thermal emission. For example, a beam-like distribution peaks in local emissivity at angles of $\sim 30^\circ$ relative to the magnetic field, which can imprint distinctive signatures on the image plane at appropriate inclinations and may even permit inference of the underlying magnetic-field geometry.

ACKNOWLEDGMENTS

We thank Yosuke Mizuno and Hongxuan Jiang for their assistance and insightful discussions. We also thank Ye Shen for his initial investigations. The work is partly supported by NSFC Grant No. 12275004, 12205013 and 12575048. M. Guo is also supported by Open Fund of Key Laboratory of Multiscale Spin Physics (Ministry of Education), Beijing Normal University.

APPENDIX

A. SUPPLEMENTARY MATERIAL FOR THE GRMHD SIMULATIONS

The top row of Fig. 12 shows the radial velocity. Before the eruption, plasma at the inner disk edge accretes at roughly $0.2c$, slower than free fall — a hallmark of the MAD state (Narayan et al. 2003). During the eruption, magnetic-energy release imparts substantial kinetic energy to the plasma, which is expelled outward at about $0.3c$, driving turbulence in the low-density region. The bottom row of Fig. 12 demonstrates distribution of electron temperature T_e . At $t = 11210 t_g$, electron temperatures in the inner disk reach $T_e \sim 10^{11} \text{K}$, produced by the conversion of gravitational potential energy into kinetic and internal energy during accretion. At the eruption peak ($t = 11330 t_g$), significant heat fluxes ($T_e \sim 10^{12} \text{K}$) appear along magnetic field lines (black arrows), especially within the low-density region. These mainly arise from the conversion of magnetic energy into kinetic and

thermal energy, consistent with the concurrent decrease in magnetic flux in Fig. 1. By $t = 11460 t_g$, these heat fluxes dissipate as the hot plasma is advected outward and mixed with the cooler external material ($T_e < 10^{10} K$), leaving only weak residual structures near the eruption site.

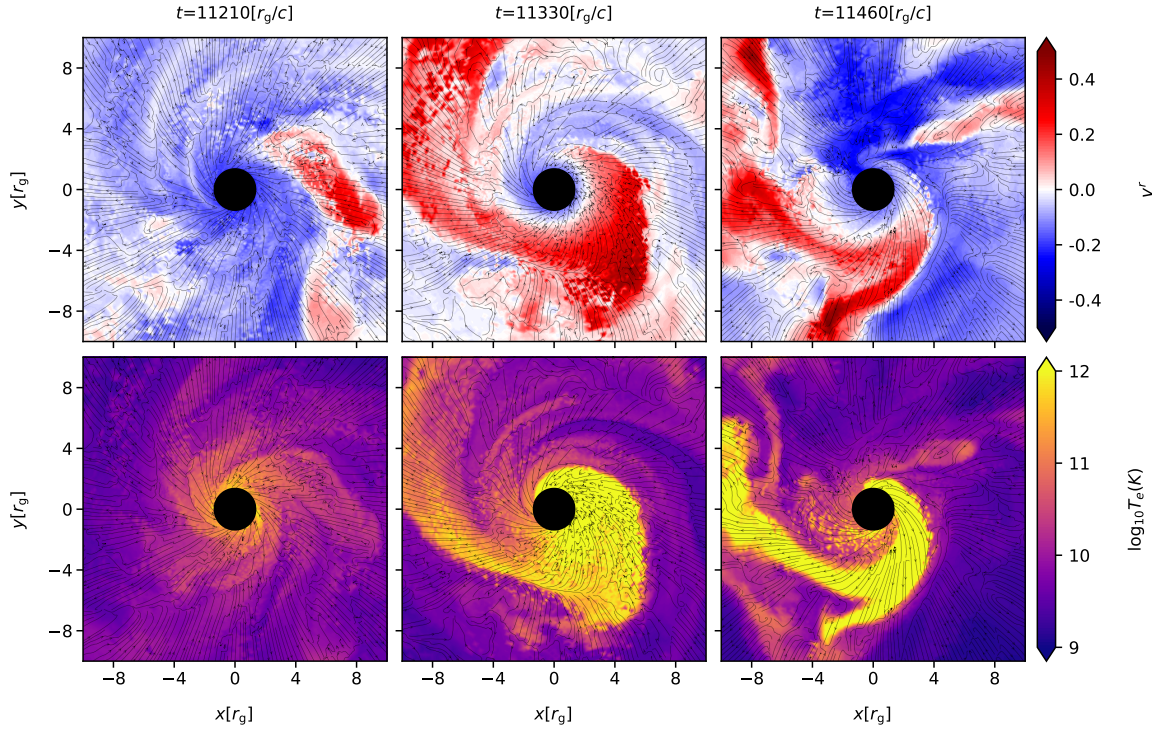


Figure 12. Distribution of radial velocity $v^r = u^r/u^t$ (**top**) and temperature T_e (**bottom**) in the $x - y$ plane at $t = 11210 t_g$, $t = 11330 t_g$ and $t = 11460 t_g$.

To further clarify the flow structure during the eruption episode, we plot in Fig. 13 the angular distributions of several key quantities at $t = 11210 t_g$, $11330 t_g$ and $11460 t_g$. Each quantity is averaged over $r \in (r_h, 10)$ and $\phi \in (0, 2\pi)$ on cones of constant θ . The top-left panel of Fig. 13 shows the θ -dependence of the plasma- β . Near the equatorial plane, the accretion flow is matter-dominated, with $\beta \simeq 10$, and the magnetic field lines are correspondingly more disordered (see Fig. 2). In contrast, the jet region has $\beta < 10^{-1}$, indicating magnetic dominance. During the eruption, we observe a modest increase in β across the disk region. The top-right panel of Fig. 13 shows the angular profile of the magnetization parameter σ_M . The jet remains strongly magnetized with $\sigma_M \gtrsim 20$. Near the equatorial plane, σ_M is initially below unity, but during the eruption it increases substantially, with values well above 1, indicating the development of a more magnetically dominated zone within the main emission region.

The bottom panels in Fig. 13 show the angular distributions of the field-line angular velocity and winding degree. The winding is quantified by the angle η_B between the toroidal and poloidal magnetic-field components, while the field-line angular velocity Ω_B characterizes how the magnetic field couples to the plasma flow and black hole rotation under ideal MHD. The original definition of Ω_B takes $\Omega_B = F_{t\theta}/F_{r\phi} = F_{t\theta}/F_{\theta\phi}$ (Blandford & Znajek 1977; Thorne & Macdonald 1982). Here, we adopt an alternative formulation appropriate for GRMHD simulations (McKinney et al. 2012). Putting these together, we have

$$\Omega_B = v^\phi - B^\phi \frac{\bar{v}_r \bar{B}_r + \bar{v}_\theta \bar{B}_\theta}{\bar{B}_r^2 + \bar{B}_\theta^2}, \quad \eta_B = \arctan \left(\frac{\bar{B}_\phi}{\sqrt{\bar{B}_r^2 + \bar{B}_\theta^2}} \right). \quad (A1)$$

Because the r and ϕ coordinates in Kerr–Schild spacetime are not orthogonal, we employ the “quasi-orthogonal” prescription (McKinney et al. 2012) to evaluate the effective magnitudes of 3-vectors along each coordinate direction. For example, for the magnetic field B^i , we define $\bar{B}_i = \sqrt{g_{ii}} B^i$ as its magnitude in the corresponding direction.

The bottom-left panel of Fig. 13 shows that in the jet region, in the jet region, Ω_B can reach $\sim 0.5 \Omega_H$, where $\Omega_H = a/(2r_h)$ is the black hole angular velocity, consistent with an efficient Blandford-Znajek process (Blandford & Znajek 1977). In the disk region,

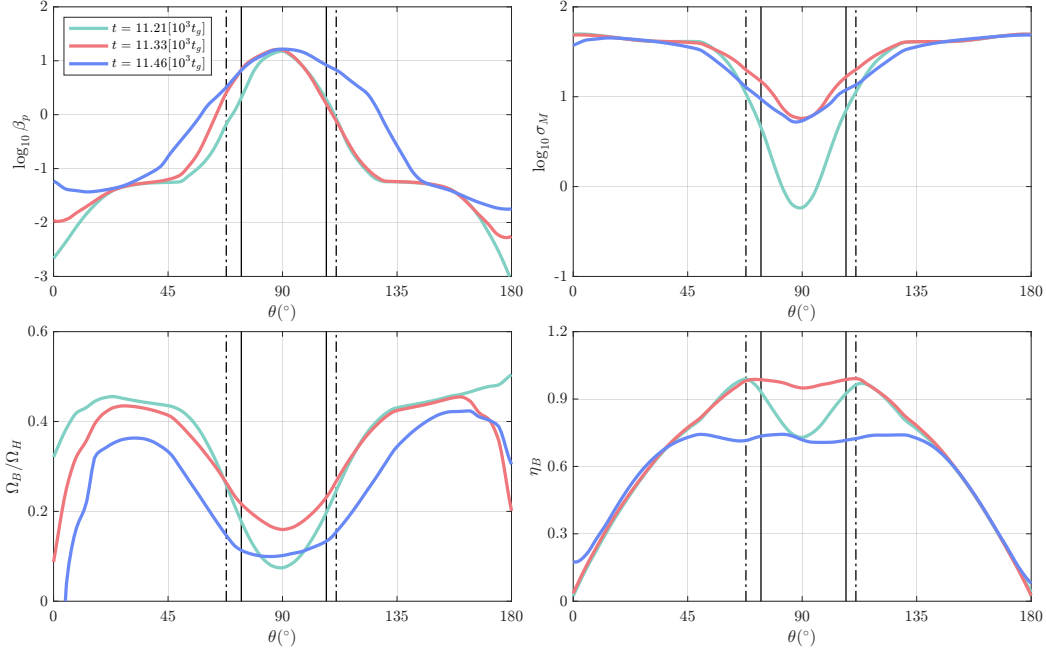


Figure 13. Variations of plasma- β (**top left**), magnetization parameter σ_M (**top right**), field-line angular velocity Ω_B (**bottom left**) and the field winding η_B (**bottom right**) as functions of θ , at $t = 11210 t_g$, $11330 t_g$ and $11460 t_g$. For each cone of constant θ , all quantities are averaged over $r \in (r_h, 10)$ and $\phi \in (0, 2\pi)$, where $r_h = M + \sqrt{M^2 - a^2}$ is the horizon radius. In each panel, the solid and dash-dotted lines mark the time- and angle-averaged contours of $-hu_t = 1.05$ and $\sigma_M = 20$, respectively.

$\Omega_B \simeq 0.1\Omega_H - 0.2\Omega_H$, primarily reflecting the sub-Keplerian rotation of the accreting matter. As magnetic flux is released and disk material is expelled, field lines previously anchored to the horizon move into the disk region, causing Ω_B there to increase from $0.1\Omega_H$ at $t = 11210 t_g$ to $0.2\Omega_H$ at $t = 11330 t_g$. In the post-eruption stage, the growing turbulence further distorts the magnetic-field configuration, leading to a latitude-wide reduction of Ω_B by about $0.1\Omega_H$.

The bottom-right panel of Fig. 13 shows the angular distribution of the field-line winding η_B . Toward the polar axis, the magnetic field becomes increasingly poloidal, as is typical for relativistic jets (Cruz-Orsio et al. 2022), whereas in the disk region the field develops a more pronounced toroidal component. Before the eruption, turbulence in the near-equatorial, matter-dominated region reduces the ϕ -averaged value of η_B , as indicated by the green curve. During the eruption, ordered field lines that thread the horizon are advected into the disk region, producing an increase in η_B there. After the eruption, the expansion of turbulence disrupts the magnetic-field structure and suppresses η_B over a broader angular range, as indicated by the purple curve.

B. NUMERICAL FRAMEWORK FOR GRRT

Building upon the **Coport** framework (Huang et al. 2024), we have optimized the numerical scheme for the radiative transfer equation to more efficiently exploit the adaptive mesh refinement (AMR) grid data produced by the BHAC code. This section presents the details of the improved numerical method. The photon trajectory is obtained by integrating the geodesic equations:

$$\frac{dx^\mu}{d\lambda} = k^\mu, \quad \frac{dk^\mu}{d\lambda} = -\Gamma^\mu_{\nu\rho} k^\nu k^\rho, \quad \frac{df^\mu}{d\lambda} = -\Gamma^\mu_{\nu\rho} k^\nu f^\rho, \quad (\text{B2})$$

where x^μ and k^μ denote the photon's position and four-momentum, respectively; $\Gamma^\mu_{\nu\rho}$ are the Christoffel symbols; and λ is the affine parameter. The vector f^μ defines a polarization basis orthogonal to k^μ and is parallel-transported along the geodesic. The evolution of the Lorentz-invariant Stokes vector takes $\vec{\mathcal{S}} = (I, Q, \mathcal{U}, \mathcal{V})$, where I is the covariant total intensity, Q, \mathcal{U} are covariant linear polarization degrees, and \mathcal{V} denotes the circular polarization degree. The evolution of $\vec{\mathcal{S}}$ is governed by the radiative transfer equation (Broderick & Blandford 2004; Shcherbakov & Huang 2011):

$$\frac{1}{C} \frac{d}{d\lambda} \begin{pmatrix} I \\ Q \\ \mathcal{U} \\ \mathcal{V} \end{pmatrix} = R(\chi) \begin{pmatrix} j_I \\ j_Q \\ 0 \\ j_V \end{pmatrix} - \left[R(\chi) \begin{pmatrix} \alpha_I & \alpha_Q & 0 & \alpha_V \\ \alpha_Q & \alpha_I & \rho_V & 0 \\ 0 & -\rho_V & \alpha_I & \rho_Q \\ \alpha_V & 0 & -\rho_Q & \alpha_I \end{pmatrix} R(-\chi) \right] \begin{pmatrix} I \\ Q \\ \mathcal{U} \\ \mathcal{V} \end{pmatrix}, \quad (\text{B3})$$

where $C = GM/c^2\nu_0$ is the dimensionless conversion factor; ν_0 denotes the photon frequency observed at infinity; j_i, α_i, ρ_i are the (invariant) emissivities, absorptivities, and Faraday coefficients. The rotation matrix $R(\chi) = R^{-1}(-\chi)$ is parameterized by the angle χ between f^μ and the local plasma magnetic field b^μ . It can be expressed in a covariant form:

$$\chi = \text{sign}(\epsilon_{\mu\nu\rho\sigma}u^\mu f^\nu b^\rho k^\sigma) \times \arccos\left(\frac{P^{\mu\nu}f_\mu b_\nu}{\sqrt{(P^{\mu\nu}f_\mu f_\nu)(P^{\alpha\beta}b_\alpha b_\beta)}}\right), \quad (\text{B4})$$

where u^μ is the fluid 4-velocity, $P^{\mu\nu}$ the induced metric on the subspace orthogonal to both u^μ and k^μ :

$$P^{\mu\nu} = g^{\mu\nu} + u^\mu u^\nu - e_k^\mu e_k^\nu, \quad e_k^\mu = \frac{k^\mu}{\nu} - u^\mu, \quad (\text{B5})$$

where $\nu = -k_\mu u^\mu$ represents the frequency of photons as observed by the co-moving fluid frame.

Given the different convergence radii and stiffness characteristics of Eqs.(B2), (B3), distinct numerical schemes are employed for each equation to improve both accuracy and convergence behavior. In particular, Eq.(B2) is integrated using an adaptive Runge–Kutta method, where the input step size $\Delta\lambda_{\text{grid}}$ is set by the AMR grid cell length Δx^i and the spatial components of the photon four-velocity k^i :

$$\Delta\lambda_{\text{grid}} = \frac{1}{n} \min\left\{\frac{\Delta x^i}{k^i}\right\}, \quad i \in \{1, 2, 3\}, \quad (\text{B6})$$

Here, n specifies the number of integration steps within each grid cell. The adaptive scheme subsequently refines $\Delta\lambda_{\text{grid}}$ to satisfy the prescribed error tolerance, yielding an effective step size $\Delta\lambda$ ($\Delta\lambda \leq \Delta\lambda_{\text{grid}}$). Once $\Delta\lambda$ is determined, the formal solution introduced in (Degl’Innocenti & Degl’Innocenti 1985) is applied to integrate Eq.(B3), thereby ensuring numerical stability and consistency of the results.

Before solving the radiative transfer equation Eq. (B3), we pre-process the variables $\mathbf{P} = \{\rho, e, \tilde{u}^i, \tilde{B}^i\}$ provided by **BHAC** (Porth et al. 2017). Here, ρ denotes the rest-mass density, e the internal energy density of the gas, $\tilde{u}^i = \Gamma v^i$ the spatial components of the four-velocity in the Eulerian frame, $\Gamma = 1/\sqrt{1 - v^2} = \sqrt{1 + \tilde{u}^2}$ the Lorentz factor, and \tilde{B}^i the magnetic field measured by an Eulerian observer. For a photon located at position \vec{X} , we identify the eight cell vertices \vec{x}_i surrounding the point and compute the linear interpolation of the primitive variables weighted by the corresponding volume fractions μ_i :

$$\bar{\mathbf{P}} = \sum_{i=1}^8 \mu_i \mathbf{P}_i, \quad \mu_i = \prod_{j=1}^3 \left(1 - \left|\frac{x_i^j - X^j}{\Delta x^j}\right|\right). \quad (\text{B7})$$

Using the interpolated primitive variables $\bar{\mathbf{P}}$, the fluid four-velocity u^μ and the magnetic four-vector b^μ are computed as follows:

$$u^\mu = \Gamma \left(\frac{1}{\alpha}, \frac{\tilde{u}^i}{\Gamma} - \frac{\beta^i}{\alpha} \right), \quad b^\mu = \left(\frac{\tilde{B}_j \tilde{u}^j}{\alpha}, \frac{\tilde{B}^i + (\tilde{B}_j \tilde{u}^j) u^i}{\Gamma} \right), \quad (\text{B8})$$

where α and β^i denote the lapse function and the shift vector in the 3+1 decomposition of spacetime, respectively. At the observer’s location, the Stokes vector $\tilde{\mathcal{S}}$ must be rotated to align with the image plane’s coordinate frame. The rotation angle χ_o is calculated by producing f^μ with the image-plane y -axis basis ($\propto -\partial_\theta^\mu$), which yields $\chi_o = \text{sign}(f^\theta) \arccos(f^\phi/f)$. The observed Stokes vector, $\tilde{\mathcal{S}}_o = (\mathcal{I}_o, \mathcal{Q}_o, \mathcal{U}_o, \mathcal{V}_o)$, is then obtained through

$$\mathcal{I}_o = \mathcal{I}, \quad \mathcal{Q}_o = \mathcal{Q} \cos \chi_o - \mathcal{U} \sin \chi_o, \quad \mathcal{U}_o = \mathcal{Q} \sin \chi_o + \mathcal{U} \cos \chi_o, \quad \mathcal{V}_o = \mathcal{V}. \quad (\text{B9})$$

C. SUPPLEMENTARY PLOTS OF THE IMAGES

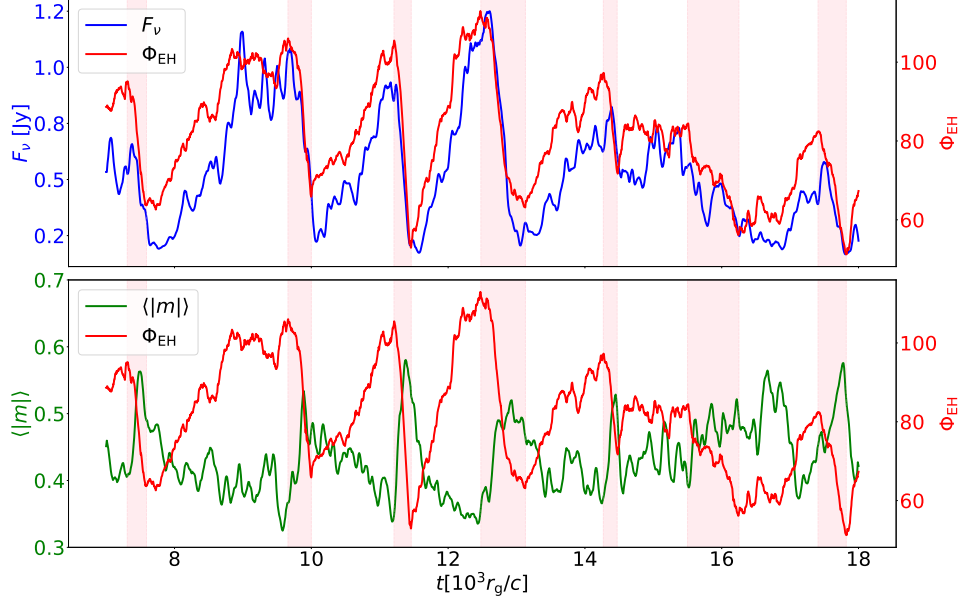


Figure 14. Time evolution of flux and linear polarization degree under thermal electron distribution for different eruption events. The variations are similar across each phase: the flux decreases with the rapid decline of magnetic flux, while the linear polarization degree increases as the magnetic flux decreases.

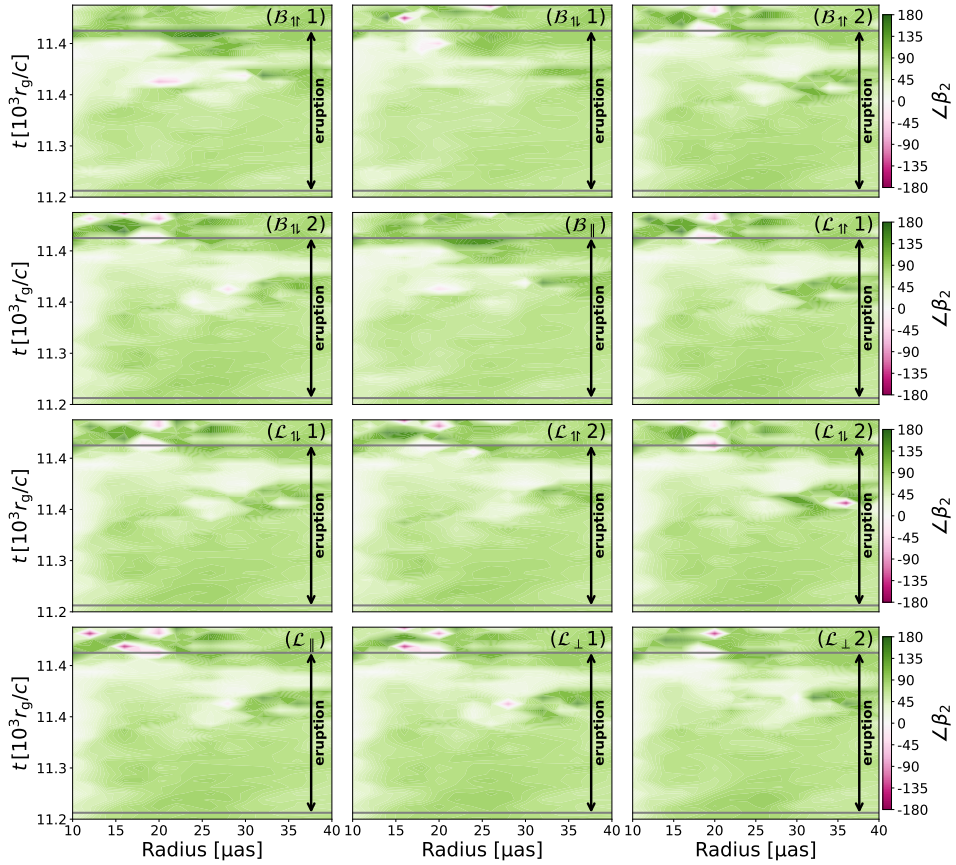


Figure 15. Radial profiles of $\arg(\beta_2)$ for anisotropic eDF models, evaluated as a function of image-plane radius and examined over different evolution times.

REFERENCES

- Abuter, R., et al. 2018, *Astron. Astrophys.*, 618, doi: [10.1051/0004-6361/201834294](https://doi.org/10.1051/0004-6361/201834294)
- . 2020, *Astron. Astrophys.*, 638, A2, doi: [10.1051/0004-6361/202037717](https://doi.org/10.1051/0004-6361/202037717)
- . 2021, *Astron. Astrophys.*, 654, A22, doi: [10.1051/0004-6361/202140981](https://doi.org/10.1051/0004-6361/202140981)
- . 2023, *Astron. Astrophys.*, 677, L10, doi: [10.1051/0004-6361/202347416](https://doi.org/10.1051/0004-6361/202347416)
- Aimar, N., Paumard, T., Vincent, F. H., Gourgoulhon, E., & Perrin, G. 2024, *Class. Quant. Grav.*, 41, 095010, doi: [10.1088/1361-6382/ad351d](https://doi.org/10.1088/1361-6382/ad351d)
- Akiyama, K., et al. 2019a, *Astrophys. J. Lett.*, 875, L1, doi: [10.3847/2041-8213/ab0ec7](https://doi.org/10.3847/2041-8213/ab0ec7)
- . 2019b, *Astrophys. J. Lett.*, 875, L5, doi: [10.3847/2041-8213/ab0f43](https://doi.org/10.3847/2041-8213/ab0f43)
- . 2019c, *Astrophys. J. Lett.*, 875, L6, doi: [10.3847/2041-8213/ab1141](https://doi.org/10.3847/2041-8213/ab1141)
- . 2019d, *Astrophys. J. Lett.*, 875, L4, doi: [10.3847/2041-8213/ab0e85](https://doi.org/10.3847/2041-8213/ab0e85)
- . 2019e, *Astrophys. J. Lett.*, 875, L2, doi: [10.3847/2041-8213/ab0c96](https://doi.org/10.3847/2041-8213/ab0c96)
- . 2019f, *Astrophys. J. Lett.*, 875, L3, doi: [10.3847/2041-8213/ab0c57](https://doi.org/10.3847/2041-8213/ab0c57)
- . 2021a, *Astrophys. J. Lett.*, 910, L12, doi: [10.3847/2041-8213/abe71d](https://doi.org/10.3847/2041-8213/abe71d)
- . 2021b, *Astrophys. J. Lett.*, 910, L13, doi: [10.3847/2041-8213/abe4de](https://doi.org/10.3847/2041-8213/abe4de)
- . 2022a, *Astrophys. J. Lett.*, 930, L12, doi: [10.3847/2041-8213/ac6674](https://doi.org/10.3847/2041-8213/ac6674)
- . 2022b, *Astrophys. J. Lett.*, 930, L15, doi: [10.3847/2041-8213/ac6736](https://doi.org/10.3847/2041-8213/ac6736)
- . 2022c, *Astrophys. J. Lett.*, 930, L16, doi: [10.3847/2041-8213/ac6672](https://doi.org/10.3847/2041-8213/ac6672)
- . 2022d, *Astrophys. J. Lett.*, 930, L17, doi: [10.3847/2041-8213/ac6756](https://doi.org/10.3847/2041-8213/ac6756)
- . 2022e, *Astrophys. J. Lett.*, 930, L13, doi: [10.3847/2041-8213/ac6675](https://doi.org/10.3847/2041-8213/ac6675)
- . 2022f, *Astrophys. J. Lett.*, 930, L14, doi: [10.3847/2041-8213/ac6429](https://doi.org/10.3847/2041-8213/ac6429)
- . 2023, *Astrophys. J. Lett.*, 957, L20, doi: [10.3847/2041-8213/acff70](https://doi.org/10.3847/2041-8213/acff70)
- . 2024a, *Astrophys. J. Lett.*, 964, L25, doi: [10.3847/2041-8213/ad2df0](https://doi.org/10.3847/2041-8213/ad2df0)
- . 2024b, *Astrophys. J. Lett.*, 964, L26, doi: [10.3847/2041-8213/ad2df1](https://doi.org/10.3847/2041-8213/ad2df1)
- . 2025, doi: [10.1051/0004-6361/202555855](https://doi.org/10.1051/0004-6361/202555855)
- Algaba, J. C., et al. 2024, *Astron. Astrophys.*, 692, A140, doi: [10.1051/0004-6361/202450497](https://doi.org/10.1051/0004-6361/202450497)
- Antonopoulou, E., Loules, A., & Nathanail, A. 2025, *Astron. Astrophys.*, 696, A10, doi: [10.1051/0004-6361/202453456](https://doi.org/10.1051/0004-6361/202453456)
- Baganoff, F. K., et al. 2001, *Nature*, 413, 45, doi: [10.1038/35092510](https://doi.org/10.1038/35092510)
- Ball, D., Sironi, L., & Özel, F. 2018, *The Astrophysical Journal*, 862, 80, doi: [10.3847/1538-4357/aac820](https://doi.org/10.3847/1538-4357/aac820)
- Bauböck, M., et al. 2020, *Astron. Astrophys.*, 635, A143, doi: [10.1051/0004-6361/201937233](https://doi.org/10.1051/0004-6361/201937233)
- Blandford, R. D., & Znajek, R. L. 1977, *Monthly Notices of the Royal Astronomical Society*, 179, 433, doi: [10.1093/mnras/179.3.433](https://doi.org/10.1093/mnras/179.3.433)
- Broderick, A., & Blandford, R. 2004, *Mon. Not. Roy. Astron. Soc.*, 349, 994, doi: [10.1111/j.1365-2966.2004.07582.x](https://doi.org/10.1111/j.1365-2966.2004.07582.x)
- Bronzwaer, T., Younsi, Z., Davelaar, J., & Falcke, H. 2020, *Astron. Astrophys.*, 641, A126, doi: [10.1051/0004-6361/202038573](https://doi.org/10.1051/0004-6361/202038573)
- Chael, A. 2024, *Mon. Not. Roy. Astron. Soc.*, 532, 3198, doi: [10.1093/mnras/stae1692](https://doi.org/10.1093/mnras/stae1692)
- Chael, A., Rowan, M. E., Narayan, R., Johnson, M. D., & Sironi, L. 2018, *Mon. Not. Roy. Astron. Soc.*, 478, 5209, doi: [10.1093/mnras/sty1261](https://doi.org/10.1093/mnras/sty1261)
- Chandra, M., Gammie, C. F., Foucart, F., & Quataert, E. 2015, *Astrophys. J.*, 810, 162, doi: [10.1088/0004-637X/810/2/162](https://doi.org/10.1088/0004-637X/810/2/162)
- Chatterjee, K., & Narayan, R. 2022, *Astrophys. J.*, 941, 30, doi: [10.3847/1538-4357/ac9d97](https://doi.org/10.3847/1538-4357/ac9d97)
- Chen, B., Hou, Y., Song, Y., & Zhang, Z. 2025, *Phys. Rev. D*, 111, 083045, doi: [10.1103/PhysRevD.111.083045](https://doi.org/10.1103/PhysRevD.111.083045)
- Comisso, L. 2024, *Astrophys. J.*, 972, 9, doi: [10.3847/1538-4357/ad51fe](https://doi.org/10.3847/1538-4357/ad51fe)
- Comisso, L., & Jiang, B. 2023, *The Astrophysical Journal*, 959, 137, doi: [10.3847/1538-4357/ad1241](https://doi.org/10.3847/1538-4357/ad1241)
- Comisso, L., & Sironi, L. 2019, *The Astrophysical Journal*, 886, 122, doi: [10.3847/1538-4357/ab4c33](https://doi.org/10.3847/1538-4357/ab4c33)
- . 2022, *The Astrophysical Journal Letters*, 936, L27
- Cruz-Orsorio, A., Fromm, C. M., Mizuno, Y., et al. 2022, *Nature Astronomy*, 6, 103, doi: [10.1038/s41550-021-01506-w](https://doi.org/10.1038/s41550-021-01506-w)
- Davelaar, J., Moscibrodzka, M., Bronzwaer, T., & Falcke, H. 2018, *Astron. Astrophys.*, 612, A34, doi: [10.1051/0004-6361/201732025](https://doi.org/10.1051/0004-6361/201732025)
- Davelaar, J., Olivares, H., Porth, O., et al. 2019, *Astron. Astrophys.*, 632, A2, doi: [10.1051/0004-6361/201936150](https://doi.org/10.1051/0004-6361/201936150)
- Davelaar, J., Ripperda, B., Sironi, L., et al. 2023, *The Astrophysical Journal Letters*, 959, L3, doi: [10.3847/2041-8213/ad0b79](https://doi.org/10.3847/2041-8213/ad0b79)
- Degl’Innocenti, E. L., & Degl’Innocenti, M. L. 1985, *Solar Physics*, 97, 239
- Dexter, J. 2016, *Mon. Not. Roy. Astron. Soc.*, 462, 115, doi: [10.1093/mnras/stw1526](https://doi.org/10.1093/mnras/stw1526)
- Dexter, J., et al. 2020, *Mon. Not. Roy. Astron. Soc.*, 497, 4999, doi: [10.1093/mnras/staa2288](https://doi.org/10.1093/mnras/staa2288)

- Dihingia, I. K., Mizuno, Y., Fromm, C. M., & Rezzolla, L. 2022, *Mon. Not. Roy. Astron. Soc.*, 518, 405, doi: [10.1093/mnras/stac3165](https://doi.org/10.1093/mnras/stac3165)
- et al., S. S. D. 2012, *Science*, 338, 355, doi: [10.1126/science.1224768](https://doi.org/10.1126/science.1224768)
- Farah, J. R., Lupsasca, A., Quataert, E., & Johnson, M. D. 2025, <https://arxiv.org/abs/2509.23628>
- Fishbone, L. G., & Moncrief, V. E. 1976, *The Astrophysical Journal*, 207, 962
- Fromm, C. M., et al. 2022, *Astron. Astrophys.*, 660, A107, doi: [10.1051/0004-6361/202142295](https://doi.org/10.1051/0004-6361/202142295)
- Galishnikova, A., Philippov, A., & Quataert, E. 2023, *Astrophys. J.*, 957, 103, doi: [10.3847/1538-4357/acfa77](https://doi.org/10.3847/1538-4357/acfa77)
- Gammie, C. F., McKinney, J. C., & Tóth, G. 2003, *The Astrophysical Journal*, 589, 444, doi: [10.1086/374594](https://doi.org/10.1086/374594)
- Gammie, C. F., & Popham, R. 1998, *The Astrophysical Journal*, 498, 313
- Genzel, R., Schodel, R., Ott, T., et al. 2003, *Nature*, 425, 934, doi: [10.1038/nature02065](https://doi.org/10.1038/nature02065)
- Ghez, A. M., Wright, S. A., Matthews, K., et al. 2004, *Astrophys. J. Lett.*, 601, L159, doi: [10.1086/382024](https://doi.org/10.1086/382024)
- Gold, R., McKinney, J. C., Johnson, M. D., & Doeleman, S. S. 2017, *Astrophys. J.*, 837, 180, doi: [10.3847/1538-4357/aa6193](https://doi.org/10.3847/1538-4357/aa6193)
- Grigorian, A. A., & Dexter, J. 2024, *Mon. Not. Roy. Astron. Soc.*, 530, 1563, doi: [10.1093/mnras/stae934](https://doi.org/10.1093/mnras/stae934)
- Hou, Y., Huang, J., Guo, M., Mizuno, Y., & Chen, B. 2025, *Astrophys. J. Lett.*, 988, L51, doi: [10.3847/2041-8213/adee09](https://doi.org/10.3847/2041-8213/adee09)
- Hou, Y., Zhang, Z., Guo, M., & Chen, B. 2024, *JCAP*, 02, 030, doi: [10.1088/1475-7516/2024/02/030](https://doi.org/10.1088/1475-7516/2024/02/030)
- Huang, J., Zheng, L., Guo, M., & Chen, B. 2024, *JCAP*, 11, 054, doi: [10.1088/1475-7516/2024/11/054](https://doi.org/10.1088/1475-7516/2024/11/054)
- Igumenshchev, I. V. 2008, *The Astrophysical Journal*, 677, 317
- Jia, H., Ripperda, B., Quataert, E., et al. 2023, *Monthly Notices of the Royal Astronomical Society*, 526, 2924, doi: [10.1093/mnras/stad2935](https://doi.org/10.1093/mnras/stad2935)
- Jiang, H.-X., Mizuno, Y., Dihingia, I. K., et al. 2024, *Astron. Astrophys.*, 688, A82, doi: [10.1051/0004-6361/202449681](https://doi.org/10.1051/0004-6361/202449681)
- . 2025, *Astrophys. J.*, 990, 81, doi: [10.3847/1538-4357/adf1e5](https://doi.org/10.3847/1538-4357/adf1e5)
- Johnson, M. D., et al. 2020, *Sci. Adv.*, 6, eaaz1310, doi: [10.1126/sciadv.aaz1310](https://doi.org/10.1126/sciadv.aaz1310)
- Jüttner, F. 1911, *Annalen der Physik*, 339, 856
- Kocherlakota, P., et al. 2021, *Phys. Rev. D*, 103, 104047, doi: [10.1103/PhysRevD.103.104047](https://doi.org/10.1103/PhysRevD.103.104047)
- Komissarov, S. 2004, *Monthly Notices of the Royal Astronomical Society*, 350, 427
- Kulsrud, R. M. 1983, *Handbook of plasma physics*, 1, 115
- . 2005, *Plasma physics for astrophysics* (Princeton University Press)
- Kunz, M. W., Schekochihin, A. A., & Stone, J. M. 2014, *Phys. Rev. Lett.*, 112, 205003, doi: [10.1103/PhysRevLett.112.205003](https://doi.org/10.1103/PhysRevLett.112.205003)
- Lai, P. C. W., Li, K. J., Yap, Y. X. J., Wu, K., & Kong, A. K. H. 2025, *Monthly Notices of the Royal Astronomical Society*, 542, 902, doi: [10.1093/mnras/staf1295](https://doi.org/10.1093/mnras/staf1295)
- Leung, P. K., Gammie, C. F., & Noble, S. C. 2011, *The Astrophysical Journal*, 737, 21
- Lupsasca, A., Cárdenas-Avendaño, A., Palumbo, D. C. M., et al. 2024, *Proc. SPIE Int. Soc. Opt. Eng.*, 13092, 130926Q, doi: [10.1117/12.3019437](https://doi.org/10.1117/12.3019437)
- Marszewski, A., Prather, B. S., Joshi, A. V., Pandya, A., & Gammie, C. F. 2021, *Astrophys. J.*, 921, 17, doi: [10.3847/1538-4357/ac1b28](https://doi.org/10.3847/1538-4357/ac1b28)
- McKinney, J. C., & Gammie, C. F. 2004, *The Astrophysical Journal*, 611, 977, doi: [10.1086/422244](https://doi.org/10.1086/422244)
- McKinney, J. C., Tchekhovskoy, A., & Blandford, R. D. 2012, *Monthly Notices of the Royal Astronomical Society*, 423, 3083, doi: [10.1111/j.1365-2966.2012.21074.x](https://doi.org/10.1111/j.1365-2966.2012.21074.x)
- Melzani, Mickaël, Walder, Rolf, Folini, Doris, Winisdoerffer, Christophe, & Favre, Jean M. 2014, *A&A*, 570, A112, doi: [10.1051/0004-6361/201424193](https://doi.org/10.1051/0004-6361/201424193)
- Mizuno, Y., Fromm, C. M., Younsi, Z., et al. 2021, *Mon. Not. Roy. Astron. Soc.*, 506, 741, doi: [10.1093/mnras/stab1753](https://doi.org/10.1093/mnras/stab1753)
- Moscibrodzka, M., Dexter, J., Davelaar, J., & Falcke, H. 2017, *Mon. Not. Roy. Astron. Soc.*, 468, 2214, doi: [10.1093/mnras/stx587](https://doi.org/10.1093/mnras/stx587)
- Moscibrodzka, M., & Falcke, H. 2013, *Astron. Astrophys.*, 559, L3, doi: [10.1051/0004-6361/201322692](https://doi.org/10.1051/0004-6361/201322692)
- Moscibrodzka, M., & Gammie, C. F. 2018, *Mon. Not. Roy. Astron. Soc.*, 475, 43, doi: [10.1093/mnras/stx3162](https://doi.org/10.1093/mnras/stx3162)
- Mościbrodzka, M., Gammie, C. F., Dolence, J. C., Shiokawa, H., & Leung, P. K. 2009, *The Astrophysical Journal*, 706, 497
- Mościbrodzka, Monika, Falcke, Heino, & Shiokawa, Hotaka. 2016, *A&A*, 586, A38, doi: [10.1051/0004-6361/201526630](https://doi.org/10.1051/0004-6361/201526630)
- Najafi-Ziyazi, M., Davelaar, J., Mizuno, Y., & Porth, O. 2024, *Mon. Not. Roy. Astron. Soc.*, 531, 3961, doi: [10.1093/mnras/stae1343](https://doi.org/10.1093/mnras/stae1343)
- Narayan, R., Igumenshchev, I. V., & Abramowicz, M. A. 2003, *Publications of the Astronomical Society of Japan*, 55, L69, doi: [10.1093/pasj/55.6.L69](https://doi.org/10.1093/pasj/55.6.L69)
- Noble, S. C., Leung, P. K., Gammie, C. F., & Book, L. G. 2007, *Classical and Quantum Gravity*, 24, S259
- Palumbo, D. C. M., Wong, G. N., & Prather, B. S. 2020, *Astrophys. J.*, 894, 156, doi: [10.3847/1538-4357/ab86ac](https://doi.org/10.3847/1538-4357/ab86ac)
- Pandya, A., Zhang, Z., Chandra, M., & Gammie, C. F. 2016, *The Astrophysical Journal*, 822, 34
- Pihajoki, P., Mannerkoski, M., Nättälä, J., & Johansson, P. H. 2018, *Astrophys. J.*, 863, 8, doi: [10.3847/1538-4357/aacea0](https://doi.org/10.3847/1538-4357/aacea0)
- Porth, O., Mizuno, Y., Younsi, Z., & Fromm, C. M. 2021, *Mon. Not. Roy. Astron. Soc.*, 502, 2023, doi: [10.1093/mnras/stab163](https://doi.org/10.1093/mnras/stab163)
- Porth, O., Olivares, H., Mizuno, Y., et al. 2017, *Computational Astrophysics and Cosmology*, 4, 1, doi: [10.1186/s40668-017-0020-2](https://doi.org/10.1186/s40668-017-0020-2)

- Porth, O., et al. 2019, *Astrophys. J. Suppl.*, 243, 26, doi: [10.3847/1538-4365/ab29fd](https://doi.org/10.3847/1538-4365/ab29fd)
- Psaltis, D., et al. 2020, *Phys. Rev. Lett.*, 125, 141104, doi: [10.1103/PhysRevLett.125.141104](https://doi.org/10.1103/PhysRevLett.125.141104)
- Pu, H.-Y., & Broderick, A. E. 2018, *Astrophys. J.*, 863, 148, doi: [10.3847/1538-4357/aad086](https://doi.org/10.3847/1538-4357/aad086)
- Quataert, E., Dorland, W., & Hammett, G. W. 2002, *The Astrophysical Journal*, 577, 524
- Ricarte, A., Palumbo, D. C. M., Narayan, R., Roelofs, F., & Emami, R. 2022, *Astrophys. J. Lett.*, 941, L12, doi: [10.3847/2041-8213/aca087](https://doi.org/10.3847/2041-8213/aca087)
- Ricarte, A., Prather, B. S., Wong, G. N., et al. 2020, *Mon. Not. Roy. Astron. Soc.*, 498, 5468, doi: [10.1093/mnras/staa2692](https://doi.org/10.1093/mnras/staa2692)
- Ripperda, B., Bacchini, F., & Philippov, A. 2020, *Astrophys. J.*, 900, 100, doi: [10.3847/1538-4357/ababab](https://doi.org/10.3847/1538-4357/ababab)
- Ripperda, B., Liska, M., Chatterjee, K., et al. 2022a, *The Astrophysical Journal Letters*, 924, L32, doi: [10.3847/2041-8213/ac46a1](https://doi.org/10.3847/2041-8213/ac46a1)
- . 2022b, *Astrophys. J. Lett.*, 924, L32, doi: [10.3847/2041-8213/ac46a1](https://doi.org/10.3847/2041-8213/ac46a1)
- Riquelme, M. A., Quataert, E., & Verscharen, D. 2015, *Astrophys. J.*, 800, 27, doi: [10.1088/0004-637X/800/1/27](https://doi.org/10.1088/0004-637X/800/1/27)
- Rybicki, G. B., & Lightman, A. P. 1979, *Lightman Radiative Processes in Astrophysics (Lightman Radiative Processes in Astrophysics)*
- Scepi, N., Dexter, J., & Begelman, M. C. 2022, *Mon. Not. Roy. Astron. Soc.*, 511, 3536, doi: [10.1093/mnras/stac337](https://doi.org/10.1093/mnras/stac337)
- Shcherbakov, R. V., & Huang, L. 2011, *Mon. Not. Roy. Astron. Soc.*, 410, 1052, doi: [10.1111/j.1365-2966.2010.17502.x](https://doi.org/10.1111/j.1365-2966.2010.17502.x)
- Tchekhovskoy, A., Narayan, R., & McKinney, J. C. 2011, *Mon. Not. Roy. Astron. Soc.*, 418, L79, doi: [10.1111/j.1745-3933.2011.01147.x](https://doi.org/10.1111/j.1745-3933.2011.01147.x)
- Thorne, K. S., & Macdonald, D. 1982, *Monthly Notices of the Royal Astronomical Society*, 198, 339
- Tsunetoe, Y., Kawashima, T., Ohsuga, K., & Mineshige, S. 2024, *Publ. Astron. Soc. Jap.*, 76, 1211, doi: [10.1093/pasj/psae083](https://doi.org/10.1093/pasj/psae083)
- Tsunetoe, Y., Pesce, D. W., Narayan, R., et al. 2025, *Astrophys. J.*, 984, 35, doi: [10.3847/1538-4357/adc37a](https://doi.org/10.3847/1538-4357/adc37a)
- Wielgus, M., Moscibrodzka, M., Vos, J., et al. 2022, *Astron. Astrophys.*, 665, L6, doi: [10.1051/0004-6361/202244493](https://doi.org/10.1051/0004-6361/202244493)
- Yang, Y.-P., & Zhang, B. 2018, *Astrophys. J. Lett.*, 864, L16, doi: [10.3847/2041-8213/aada4f](https://doi.org/10.3847/2041-8213/aada4f)
- Younsi, Z., Porth, O., Mizuno, Y., Fromm, C. M., & Olivares, H. 2020, *IAU Symp.*, 342, 9, doi: [10.1017/S1743921318007263](https://doi.org/10.1017/S1743921318007263)
- Zhang, M., Mizuno, Y., Fromm, C. M., Younsi, Z., & Cruz-Orsio, A. 2024a, *Astron. Astrophys.*, 687, A88, doi: [10.1051/0004-6361/202449497](https://doi.org/10.1051/0004-6361/202449497)
- Zhang, Z., Hou, Y., Guo, M., & Chen, B. 2024b, *JCAP*, 05, 032, doi: [10.1088/1475-7516/2024/05/032](https://doi.org/10.1088/1475-7516/2024/05/032)
- Zhao, J.-H., Bower, G. C., & Goss, W. M. 2001, *Astrophys. J. Lett.*, 547, L29, doi: [10.1086/318877](https://doi.org/10.1086/318877)